The Astronomical Journal, 146:21 (17pp), 2013 August doi:10.1088/0004-6256/146/2/21
© 2013. The American Astronomical Society. All rights reserved. Printed in the U.S.A.

EXPLORING THE VARIABLE SKY WITH LINEAR. II. HALO STRUCTURE AND SUBSTRUCTURE TRACED BY RR LYRAE STARS TO 30 kpc

Branimir Sesar[1], Željko Ivezić[2], J. Scott Stuart[3], Dylan M. Morgan[2], Andrew C. Becker[2], Sanjib Sharma[4], Lovro Palaversa[5], Mario Jurić[6,7], Przemyslaw Wozniak[8], and Hakeem Oluseyi[9]
[1] Division of Physics, Mathematics and Astronomy, Caltech, Pasadena, CA 91125, USA
[2] University of Washington, Department of Astronomy, P.O. Box 351580, Seattle, WA 98195-1580, USA
[3] Lincoln Laboratory, Massachusetts Institute of Technology, 244 Wood Street, Lexington, MA 02420-9108, USA
[4] Sydney Institute for Astronomy, School of Physics, University of Sydney, NSW 2006, Australia
[5] Observatoire astronomique de l'Université de Genève, 51 chemin des Maillettes, CH-1290 Sauverny, Switzerland
[6] Steward Observatory, University of Arizona, Tucson, AZ 85121, USA
[7] LSST Corporation, 933 North Cherry Avenue, Tucson, AZ 85721, USA
[8] Los Alamos National Laboratory, 30 Bikini Atoll Rd., Los Alamos, NM 87545-0001, USA
[9] Florida Institute of Technology, Melbourne, FL 32901, USA
Received 2013 February 3; accepted 2013 May 8; published 2013 June 27

ABSTRACT

We present a sample of ∼5000 RR Lyrae stars selected from the recalibrated LINEAR data set and detected at heliocentric distances between 5 kpc and 30 kpc over ∼8000 deg^2 of sky. The coordinates and light curve properties, such as period and Oosterhoff type, are made publicly available. We analyze in detail the light curve properties and Galactic distribution of the subset of ∼4000 type ab RR Lyrae (RRab) stars, including a search for new halo substructures and the number density distribution as a function of Oosterhoff type. We find evidence for the Oosterhoff dichotomy among field RR Lyrae stars, with the ratio of the type II and I subsamples of about 1:4, but with a weaker separation than for globular cluster stars. The wide sky coverage and depth of this sample allow unique constraints for the number density distribution of halo RRab stars as a function of galactocentric distance: it can be described as an oblate ellipsoid with an axis ratio $q = 0.63$ and with either a single or a double power law with a power-law index in the range −2 to −3. Consistent with previous studies, we find that the Oosterhoff type II subsample has a steeper number density profile than the Oosterhoff type I subsample. Using the group-finding algorithm EnLink, we detected seven candidate halo groups, only one of which is statistically spurious. Three of these groups are near globular clusters (M53/NGC 5053, M3, M13), and one is near a known halo substructure (Virgo Stellar Stream); the remaining three groups do not seem to be near any known halo substructures or globular clusters and seem to have a higher ratio of Oosterhoff type II to Oosterhoff type I RRab stars than what is found in the halo. The extended morphology and the position (outside the tidal radius) of some of the groups near globular clusters are suggestive of tidal streams possibly originating from globular clusters. Spectroscopic follow-up of detected halo groups is encouraged.

Key words: Galaxy: halo – Galaxy: stellar content – Galaxy: structure – stars: variables: RR Lyrae

Online-only material: animation, color figures, machine-readable and VO tables, supplemental data (FITS) file (tar.gz)

1. INTRODUCTION

Studies of the Galactic halo provide unique insights into the formation history of the Milky Way, and the galaxy formation process in general (Helmi 2008). One of the main reasons for this uniqueness is that dynamical timescales are much longer than for disk stars and thus the "memory of past events lasts longer" (e.g., Johnston et al. 1996; Mayer et al. 2002). For example, within the framework of hierarchical galaxy formation (Freeman & Bland-Hawthorn 2002), the spheroidal component of the luminous matter should reveal substructures such as tidal tails and streams (Johnston et al. 1996; Helmi & White 1999; Bullock et al. 2001; Harding et al. 2001). The amount of substructures and the distribution of their properties such as mass and radial distance can be used to place constraints on the accretion history of the Galaxy (Johnston et al. 2008; Sharma et al. 2011). The number of these substructures, created due to mergers and accretion over the Galaxy's lifetime, may provide a crucial test for proposed solutions to the "missing satellite" problem (Bullock et al. 2001). Substructures are expected to be ubiquitous in the outer halo (galactocentric distance >15–20 kpc), and indeed many have been discovered (for a recent review, see Ivezić et al. 2012). Understanding the number density distribution of stars (i.e., the structure) in the halo is equally important because its shape and profile affect estimates of the degree of velocity anisotropy and estimates of the mass of the Milky Way (Deason et al. 2012; Kafle et al. 2012). Various luminous tracers, such as main-sequence turn-off stars, RR Lyrae variables, blue horizontal branch (BHB) stars, and red giants, are used to map halo structure and substructures; among them, RR Lyrae stars have proven to be especially useful.

RR Lyrae stars represent a fair sample of the old halo population (Smith 2004). They are nearly standard candles, are sufficiently bright to be detected at large distances, and are sufficiently numerous to trace the halo substructures with good spatial resolution (Sesar et al. 2010a). Fairly complete and relatively clean samples of RR Lyrae stars can be selected using single-epoch colors (Ivezić et al. 2005) and, if multi-epoch data exist, using variability (Ivezić et al. 2000; QUEST, Vivas et al. 2001; Sesar et al. 2007; De Lee 2008; SEKBO, Keller et al. 2008; LONEOS-I, Miceli et al. 2008). A useful comparison of recent RR Lyrae surveys in terms of their sky coverage, distance

limits, and sample size is presented by Keller et al. (2008, see their Table 1).

As an example of the utility of RR Lyrae samples, the period and amplitude of their light curves may hold clues about the formation history of the Galactic halo (Catelan 2009). The distribution of RR Lyrae stars in globular clusters in the period–amplitude diagram displays a dichotomy, first noted by Oosterhoff (1939). According to Catelan (2009), if the Galactic halo was entirely built from smaller "protogalactic fragments" like the present-day Milky Way dwarf spheroidal (dSph) satellite galaxies, the halo should not display this so-called Oosterhoff dichotomy (see Section 4 for details) because the dSph galaxies and their globular clusters are predominantly intermediate between the two Oosterhoff classes. Whether the present-day halo displays the Oosterhoff dichotomy is still a matter of contention. Some studies claim detection of distinct Oosterhoff type I (Oo I) and Oosterhoff type II (Oo II) components (Miceli et al. 2008; De Lee 2008; Szczygieł et al. 2009), while others do not see a clear Oo II component (Kinemuchi et al. 2006).

In order to determine the Oosterhoff class for an RR Lyrae star, a well-sampled light curve is needed. Most of the above studies used RR Lyrae stars selected from surveys that were either deep with small sky coverage (e.g., 300 deg^2 large SDSS Stripe 82; De Lee 2008; Watkins et al. 2009; Sesar et al. 2010a), or shallow with wide sky coverage (e.g., ASAS; Szczygieł et al. 2009). LINEAR is a wide-area survey that provides both depth and a large area[10]; RR Lyrae stars from LINEAR are detected to the edge of the inner halo (∼30 kpc) over a sky area of ∼8000 deg^2. The main goals of this paper are to (1) present a sample of ∼5000 RR Lyrae stars selected from the LINEAR database, and (2) quantify their spatial distribution and the differences, if any, between the behavior of the two Oosterhoff classes.

This paper is the second one in a series based on light curve data collected by the LINEAR asteroid survey. In the first paper, Sesar et al. (2011b) described the LINEAR survey and photometric recalibration based on SDSS stars acting as a dense grid of standard stars. In the overlapping ∼10,000 deg^2 of sky between LINEAR and SDSS, Sesar et al. obtained photometric errors of 0.03 mag for sources not limited by photon statistics, with errors rising to 0.2 mag at $r \sim 18$. LINEAR data provide time domain information for the brightest four magnitudes of the SDSS survey, with 250 unfiltered photometric observations per object on average (rising to ∼500 along the ecliptic). Public access to the recalibrated LINEAR data, including over 5 billion photometric measurements for about 25 million objects (about three quarters are stars) is provided through the SkyDOT Web site (https://astroweb.lanl.gov/lineardb/). Positional matches to SDSS and 2MASS (Skrutskie et al. 2006) catalog entries are also available for the entire sample.

The selection criteria for RR Lyrae stars and analysis of the contamination and completeness of the resulting sample are described in Section 2. Estimation of the light curve parameters and distance determination are discussed in Section 3, and the period–amplitude distribution in Section 4. The spatial distribution of the resulting samples is quantified in Section 5, and the search for halo substructures is presented in Section 6. Our results are discussed and summarized in Section 7.

[10] While this paper was in preparation, the first analysis of ∼12,000 RR Lyrae stars selected from half of the sky monitored by the Catalina Survey was reported by Drake et al. (2013). For a comparison of their results and our work, see Section 7.

2. SELECTION OF RR LYRAE STARS

In this section, we describe the method used to select RR Lyrae stars from the recalibrated LINEAR data set. The selection method is fine-tuned using a training set of known RR Lyrae stars selected by Sesar et al. (2010a, hereafter Ses10) from the SDSS Stripe 82 region. Even though this training set is estimated to be essentially complete (∼99%; Süveges et al. 2012) and contamination-free, we confirm these estimates in Sections 2.3 and 2.4. In the context of this work, the sample completeness is defined as the fraction of RR Lyrae stars recovered as a function of magnitude, and the contamination is defined as the fraction of non-RR Lyrae stars in a sample.

We start initial selection by selecting point-like (SDSS objtype = 6) objects from the LINEAR database that:

1. are located in the region of the sky defined by $309^\circ <$ R.A. $< 60^\circ$ and $|\mathrm{Decl.}| < 1\overset{\circ}{.}23$, where both SDSS Stripe 82 and LINEAR have uniform coverage,
2. have light curves with at least 15 good observations in LINEAR (nPtsGood $\geqslant 15$), and
3. have single-epoch SDSS colors (corrected for extinction using the Schlegel et al. 1998 dust map) in these ranges:

$$0.75 < u - g < 1.45 \quad (1)$$

$$-0.25 < g - r < 0.4 \quad (2)$$

$$-0.2 < r - i < 0.2 \quad (3)$$

$$-0.3 < i - z < 0.3. \quad (4)$$

The last criterion limits the acceptable range of single-epoch SDSS colors that a candidate RR Lyrae star may have (Sesar et al. 2010a). Using a sample of ∼500 RR Lyrae stars from the SDSS Stripe 82 region, Ses10 have shown that Equations (1)–(4) encompass the full range of SDSS colors that an RR Lyrae star may have, irrespective of the phase. Therefore, by considering LINEAR objects with these single-epoch SDSS colors we eliminate most non-RR Lyrae stars, and still select all true RR Lyrae stars. The last criterion reduces the sample of candidates by a factor of eight to 90,897 candidates.

2.1. Light Curve Analysis

In the next step, we use an implementation of the *Supersmoother* algorithm (Friedman 1984; Reimann 1994) to find five most likely periods of variability for the 90,897 LINEAR objects that pass the above cuts. For 22,117 candidate RR Lyrae stars, Supersmoother returns one or more periods in the 0.2–0.9 day range (typical of RR Lyrae stars; Smith 2004); the curves are phased (period-folded) with each period and a set of SDSS r-band templates from Ses10 are fitted to phased data.

Even though LINEAR cameras observe without a spectral filter, the choice of SDSS r-band templates for light curve fitting is an appropriate one. As shown in Figure 4 from Sesar et al. (2011b), the color term between the LINEAR magnitude and SDSS r-band magnitude is essentially independent of color for blue stars such as RR Lyrae stars (∼0.02 mag within $0 < g - i < 0.5$). This means that the shapes of RR Lyrae light curves in the LINEAR and SDSS r-band will be identical for all practical purposes (especially so given the systematic error in LINEAR magnitudes of ∼0.03 mag and rapidly increasing photometric uncertainty at magnitudes fainter than 15 mag; see Figure 12 in Sesar et al. 2011b).

The light-curve fitting to estimate the best period and template is performed by minimizing the robust goodness-of-fit cost function defined in Equation (5) in the least-square sense, with the heliocentric Julian date (HJD) of peak brightness HJD_0, peak-to-peak amplitude A, and peak brightness m_0 as free parameters. The quality of a template fit is defined with a χ^2-like parameter (L_1 norm)

$$\zeta = \mathrm{median}\left(|m^i_{\mathrm{observed}} - m_{\mathrm{template}}|/\epsilon^i_{\mathrm{observed}}\right), \quad (5)$$

where m_{observed} and $\epsilon_{\mathrm{observed}}$ are the observed magnitude and its uncertainty, m_{template} is the magnitude predicted by the template, and $i = 1, N_{\mathrm{obs}}$, where N_{obs} is the number of observations. Here we use the median to minimize the bias in ζ due to rare observations with anomalous (non-Gaussian) errors (e.g., due to image artifacts, cosmic rays). The template with the lowest ζ value is selected as the best fit, and the best-fit parameters are stored.

In addition to these parameters, we also estimate the shape of the folded light curve using the skewness of the distribution of the medians of magnitudes binned in phase bins (binned 0.1 in phase). We find this skewness (hereafter γ) to be more robust than the skewness calculated using all data points (not binned in phase), because it reduces the impact of uneven sampling and filters out observations that may have unreliable errors (e.g., due to image artifacts, cosmic rays).

2.2. Optimization of the Selection Criteria for RR Lyrae Stars

At the end of the template fitting step, each light curve is characterized with the following parameters: χ^2 per degree of freedom χ^2_{pdf}, number of good LINEAR observations nPtsGood, period of variability P, peak-to-peak amplitude A, peak brightness m_0, and light-curve skewness γ. The next step is to find the right combination of cuts on these parameters that yields a sample with as high as possible completeness and as low as possible contamination for *both* type ab and type c RR Lyrae stars (RRab and RRc; i.e., the selection is not optimized for either type). The virtually complete and contamination-free sample of RR Lyrae stars selected by Ses10 greatly simplifies this process.

For a given trial set of cuts, we tag LINEAR candidates that pass these cuts as RR Lyrae stars, while those that do not pass cuts are tagged as non-RR Lyrae stars. The tagged candidates are then positionally matched to the SDSS Stripe 82 sample of RR Lyrae stars to confirm whether the tagging was correct or not.

We have found that the following cuts offer the best trade-off between contamination and completeness (2% contamination and 80% completeness for objects brighter than ∼18 mag; see Sections 2.4 and 2.5):

$$\chi^2_{\mathrm{pdf}} > 1 \quad (6)$$

$$\mathrm{nPtsGood} > 100 \quad (7)$$

$$-0.6 < \log(P/\mathrm{day}) < -0.046 \quad (8)$$

$$A > 0.3\,\mathrm{mag} \quad (9)$$

$$m_0 < 17.8\,\mathrm{mag} \quad (10)$$

$$-1 < \gamma < 0.2. \quad (11)$$

The $\chi^2_{\mathrm{pdf}} > 1$, nPtsGood > 100, and $m_0 < 17.8$ mag cuts were motivated by properties of the LINEAR data set (e.g., the LINEAR faint limit is at ∼18 mag and the median number of non-flagged observations per object is ∼200; Sesar et al. 2011b), while the cuts on amplitude, period, and skewness were motivated by light curve properties of RR Lyrae stars (e.g., see Figure 11 in Sesar et al. 2007 and Figure 16 in Sesar et al. 2011b). In total, the above criteria tag 226 objects from SDSS Stripe 82 that also have LINEAR light curves as RR Lyrae stars.

2.3. Contamination in the Sesar et al. (2010a) Sample of RR Lyrae Stars

In Sections 2.4 and 2.5, the Ses10 sample of RR Lyrae stars is used as the "ground truth" when estimating the efficiency of the above selection algorithm. Before proceeding further, it seems prudent to verify the level of contamination in this "ground truth" sample using more numerous observations provided by the LINEAR data set.

The key factor that influences the classification of an object is its period. If the period is incorrect, a true RR Lyrae star may be rejected or a non-RR Lyrae star may be accepted. Thus, a good starting point for finding possible contaminants is to search for objects that have different periods when derived from different light curve data sets.

To check for contamination by non-RR Lyrae stars in the Ses10 sample of RR Lyrae stars, we compare two sets of phased LINEAR light curves of Ses10 RR Lyrae stars. The first set is phased with periods derived from LINEAR data, and the second set is phased with periods derived from SDSS Stripe 82 data. For most bright ($m_0 < 17$) and well-sampled LINEAR objects, the LINEAR and SDSS periods agree within a root-mean-square (rms) scatter of 0.3 s. However, there are two Stripe 82 objects (RR Lyrae ID 747380 and 1928523 from Ses10) for which the LINEAR period provides a much smoother phased light curve than the period derived from SDSS Stripe 82 data. These LINEAR periods are much shorter than the SDSS periods (∼0.28 days versus ∼0.6 days), and challenge the initial RR Lyrae classification of the two objects.

After a visual inspection of their phased light curves, shown in Figure 1, we conclude that these objects are likely RRc stars instead of RRab stars as originally classified by Ses10. Even though the classification changed from one RR Lyrae type to another, these stars are still RR Lyrae stars and should not be considered contaminants in the Ses10 sample. Based on this analysis, we confirm our initial assumption that the Ses10 sample is essentially free of contamination.

2.4. Contamination in the LINEAR Sample of RR Lyrae Stars

The contamination, or the fraction of non-RR Lyrae stars in a sample of candidate RR Lyrae stars, is an important quantity that needs to be known (and minimized) before the Galactic halo is mapped. As an illustration of the impact of contamination on Galactic halo number density maps, consider RR Lyrae samples obtained by Sesar et al. (2007) and Ses10. Due to the smaller number of epochs available at the time, the Sesar et al. (2007) sample of RR Lyrae stars had a higher contamination than a more recent sample constructed by Ses10 (∼30% versus close to zero contamination in Ses10). The result of contamination in the Sesar et al. (2007) sample was the appearance of false halo overdensities in their halo number density maps (e.g., overdensities labeled D, F, H, I, K, and L in Figure 13 by Sesar et al. 2007), which are not present in density maps obtained using a much cleaner Ses10 sample (see Figure 11 by Ses10). These false overdensities observed by Sesar et al. (2007)

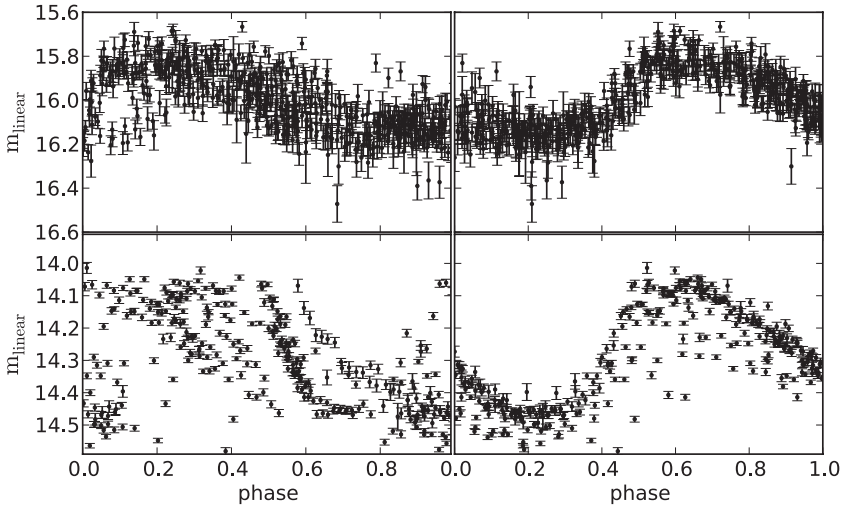

Figure 1. Comparison of LINEAR light curves phased using periods derived from SDSS (left) and LINEAR data (right). The LINEAR light curves for Sesar et al. (2010a) RR Lyrae with IDs 747380 and 1928523 are shown in top and bottom panels, respectively. For these two stars, the LINEAR periods seem to be more accurate since the light curves phased using LINEAR periods, shown on the right, are smoother than light curves phased using SDSS periods. The LINEAR periods are much shorter than SDSS periods (∼0.28 days vs. ∼0.6 days) indicating that the two stars are more likely to be type c RR Lyrae stars and not type ab RR Lyrae stars as originally classified by Sesar et al. (2010a).

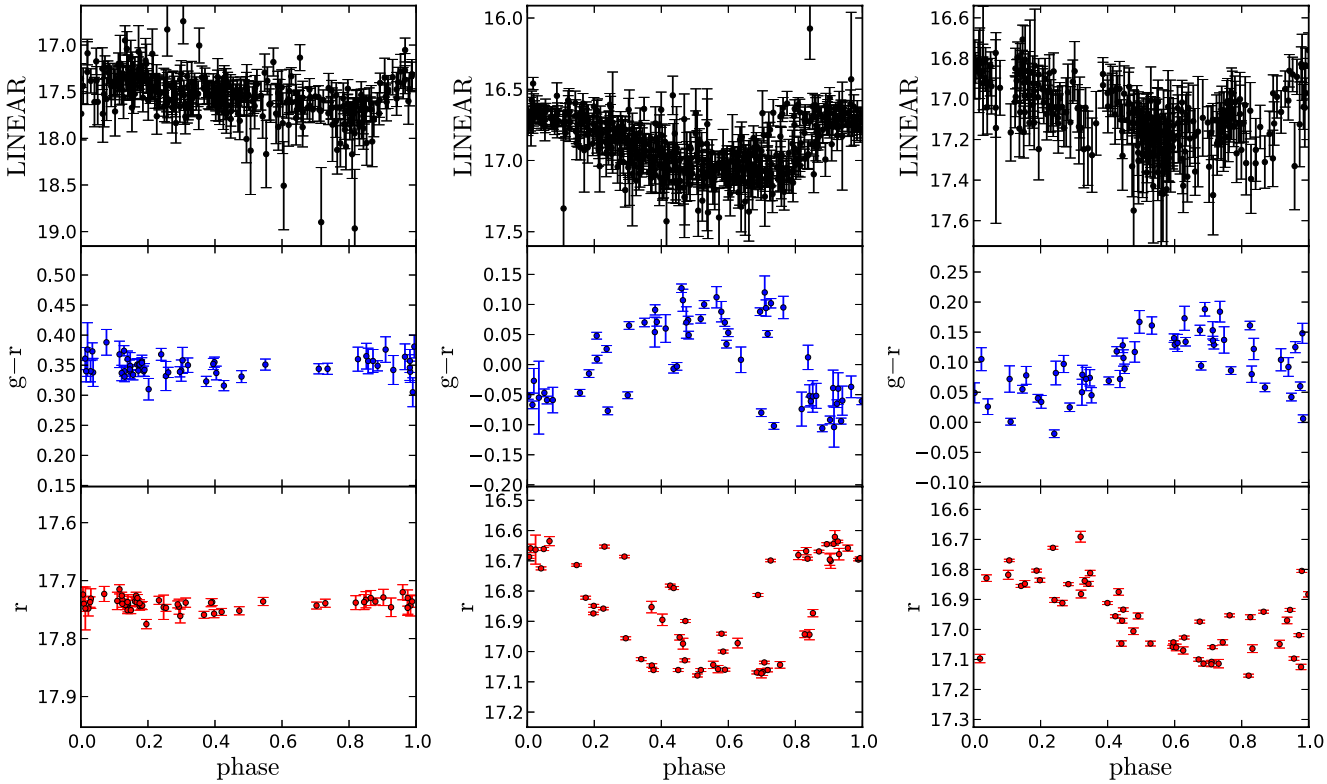

Figure 2. LINEAR and SDSS $g-r$ and r-band light curves of some objects tagged as RR Lyrae stars based on LINEAR data, but not tagged as RR Lyrae stars by Sesar et al. (2010a). The object on the left is clearly not an RR Lyrae star, and it was most likely falsely tagged as an RR Lyrae star due to its noisy LINEAR data. There are three more objects with noisy LINEAR light curves that were tagged as RR Lyrae stars, but they are not shown in this plot. The object in the middle is possibly a Blažko or a double-mode (type d) RR Lyrae star, and the object on the right is probably a variable non-RR Lyrae star.

(A color version of this figure is available in the online journal.)

consist of variable, non-RR Lyrae stars (mainly δ Scuti stars), which were projected in distance far into the halo due to the incorrect assignment of absolute magnitudes (i.e., $M_V = 0.6$ mag typical of RR Lyrae stars was assigned when the true absolute magnitude value is much lower).

Out of 226 LINEAR objects tagged as RR Lyrae stars in the SDSS Stripe 82 by our selection algorithm, only 6 (or ∼3%) are not in the Ses10 Stripe 82 sample of RR Lyrae stars. One possibility is that these objects are non-RR Lyrae stars. Alternatively, some or all of them may be true RR Lyrae stars that were overlooked by Ses10 and therefore were not included in their final sample (i.e., the Ses10 sample may not be complete). To find whether any of these six stars are RR Lyrae stars, we phase their LINEAR and SDSS g- and r-band observations using the best-fit period determined from LINEAR data, and plot their phased light curves in Figure 2 for visual inspection.

Their phased light curves reveal that four out six objects have noisy LINEAR light curves (objects are faint and have $m_0 > 17$ mag), and show no significant variability in SDSS data. Noisy LINEAR light curves are the most likely reason why these spurious, non-variable objects end up in our RR Lyrae sample. The remaining two objects show significant variability in SDSS data: one is possibly a Blažko or a double-mode (type d) RR Lyrae star while the other variable object is probably not an RR Lyrae star.

The above analysis suggests that our selection algorithm produces an RR Lyrae sample where only up to ∼2% of objects are non-RR Lyrae stars. The majority of contaminants are spurious, non-variable objects with noisy LINEAR data. Since the RR Lyrae sample is mostly contaminated at the faint end, special attention needs to be given to distant halo overdensities as these are more likely to contain non-RR Lyrae stars and are therefore more likely to be spurious. This analysis also suggests that the completeness of the Ses10 sample is very high, with plausibly only one RR Lyrae star missed by Ses10 in the range $r < 17$ (the magnitude range probed by LINEAR).

2.5. Completeness of the LINEAR Sample of RR Lyrae Stars

The completeness, or the fraction of RR Lyrae stars recovered as a function of magnitude, is another important quantity that needs to be understood before the spatial distribution of RR Lyrae stars can be analyzed. To quantify completeness, we again use the Ses10 sample of RR Lyrae stars as the "ground truth" and assume the sample is complete and clean based on the analyses presented in the previous two subsections.

The completeness as a function of peak magnitude m_0 is defined as the ratio

$$f_{\rm completeness}(m_0) = N_{\rm selected}(m_0)/N_{\rm all}(m_0), \qquad (12)$$

where $N_{\rm selected}$ is the number of SDSS Stripe 82 RR Lyrae stars that have been tagged by our selection algorithm and $N_{\rm all}$ is the number of all SDSS Stripe 82 RR Lyrae stars in a magnitude bin centered on m_0. The peak brightness of an SDSS Stripe 82 RR Lyrae star in the LINEAR photometric system (m_0) is calculated using its best-fit peak brightness in the SDSS r-band light curve (r_0; see Table 2 in Sesar et al. 2010a) as

$$m_0 = r_0 + 0.0574, \qquad (13)$$

where the 0.0574 mag offset accounts for a small magnitude zero-point shift between SDSS and LINEAR photometric systems (see Equation (6) in Sesar et al. 2011b). A comparison of synthetic and observed m_0 values shows that the two are similar within 0.04 mag, as estimated by their rms scatter.

The two types of RR Lyrae stars show a different dependence of completeness on peak magnitude m_0, as illustrated in Figure 3. While the completeness of RRab stars is estimated at ∼80% and is seemingly independent of magnitude for $m_0 < 17.2$ (corresponding to heliocentric distances from 5 kpc to 23 kpc), the completeness of RRc shows a strong dependence on magnitude, with low completeness at the bright and faint ends, and a peak at $m_0 \sim 16.2$ (but note the size of Poisson error bars).

Detailed analysis has demonstrated that the amplitude cut $A > 0.3$ mag, together with low typical amplitudes of RRc stars ($A \sim 0.3$ mag; see Figure 4) are the main reasons for low completeness of RRc stars (the increase in completeness of RRc stars toward $m_0 \sim 16.2$ is likely due to Poisson noise). We could have lowered the cut on amplitude to include more RRc stars, but that would then increase the overall contamination of the more numerous RRab sample, which we wanted to keep low per discussion in Section 2.4.

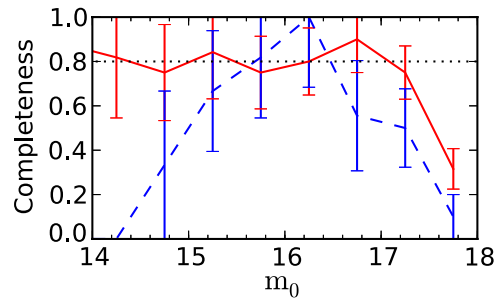

Figure 3. Completeness, or the fraction of RR Lyrae stars recovered as a function of magnitude for type ab (solid) and type c (dashed) RR Lyrae stars selected in LINEAR. The sample of type ab RR Lyrae stars is about 80% complete between 5 and 23 kpc ($14 < m_0 < 17.2$), but do note the Poisson error bars.

(A color version of this figure is available in the online journal.)

3. LINEAR CATALOG OF RR LYRAE STARS

There are 533,189 point-like (SDSS objtype = 6) objects in the LINEAR database that satisfy conditions given by Equations (1)–(4) and (6)–(7). Out of this sample, we have selected 4067 RRab and 834 RRc stars following the procedure described in Section 2. Equatorial J2000.0 right ascension and declination of selected RRab and RRc stars are listed[11] in Table 1. For a catalog of RR Lyrae stars in SDSS Stripe 82, we instead suggest the more complete and deeper Ses10 catalog be used.

3.1. Final Estimation of Light Curve Parameters

Visual inspection of phased light curves has revealed that a non-negligible number of LINEAR RR Lyrae stars have underestimated best-fit light curve amplitudes. As shown in the top plot of Figure 5, some of these stars have two or more different maxima and are most likely undergoing light curve modulations (i.e., the Blažko effect; Blažko 1907; Buchler & Kolláth 2011). Determining the true amplitude of such stars may not even be possible as the Blažko cycle does not always repeat regularly (Chadid et al. 2010; Kolenberg et al. 2011; Sódor et al. 2011).

In other cases (bottom plot in Figure 5), the light curve amplitude is underestimated because the best-fit template does not adequately model the observed light curve. That some light curves are not adequately modeled is expected because the light curve template set provided by Ses10 is not all-inclusive (see Figure 7 in Ses10). This inadequate modeling does not affect the selection procedure as the quality of a template fit (ζ parameter; see Equation (5)) is not used during selection. The amplitudes, which are used during selection, are underestimated only for RRab stars with light curve amplitudes greater than 0.5 mag, and such stars are already above the $A > 0.3$ mag selection cut (Equation (9)). However, inadequate light curve modeling is a problem as amplitudes (used in Section 4) and flux-averaged magnitudes (used in Section 3.2) are derived from best-fit model light curves.

We address the issue of inadequate template fits by re-fitting LINEAR RR Lyrae light curves with new templates created from the LINEAR RR Lyrae light curve set itself, following

[11] Note that this catalog does not contain RR Lyrae stars that are located in SDSS Stripe 82 region.

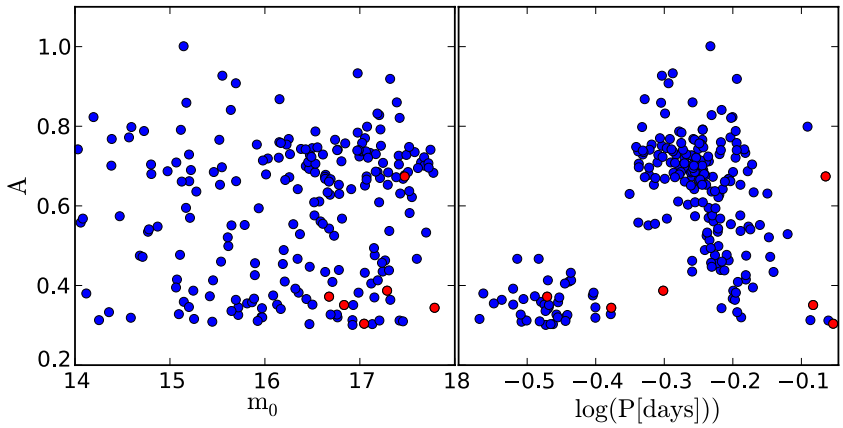

Figure 4. Distribution of LINEAR objects tagged as RR Lyrae stars in amplitude vs. peak brightness (left) and amplitude vs. period diagrams (right). LINEAR objects present in the Sesar et al. (2010a) sample of RR Lyrae stars are shown as blue dots, while those not found in the Sesar et al. (2010a) sample are shown as red dots. The LINEAR and SDSS Stripe 82 light curves of objects shown as red dots are compared in Figure 2.

(A color version of this figure is available in the online journal.)

Table 1
Positions and Light Curve Parameters of LINEAR RR Lyrae Stars

LINEAR ObjectID[a]	R.A.[b] (deg)	Decl.[b] (deg)	Type	Period (day)	HJD_0[c] (day)	Amplitude[d] (mag)	m_0[e] (mag)	Template ID[f]	rExt[g] (mag)	$\langle m \rangle$[h] (mag)	Distance[i] (kpc)	Oosterhoff Class[j]	Group ID[k]
29848	119.526418	46.962232	ab	0.557021	53802.775188	0.598	16.020	4068023	0.145	16.129	12.76	1	0
32086	119.324018	47.095636	ab	0.569258	53774.779119	0.721	14.535	32086	0.186	14.705	6.62	1	0

Notes.
[a] Identification number referencing this object in the LINEAR database. ObjectIDs of RR Lyrae stars taken from the LINEAR Catalog of Variable Stars (Palaversa et al. 2013) end with a "*" symbol.
[b] Equatorial J2000.0 right ascension and declination.
[c] Reduced heliocentric Julian date of maximum brightness ($HJD_0 - 2400000$).
[d] Amplitude measured from the best-fit LINEAR template.
[e] Maximum brightness measured from the best-fit LINEAR template (not corrected for interstellar medium extinction).
[f] Best-fit LINEAR template ID number.
[g] Extinction in the SDSS r band calculated using the Schlegel et al. (1998) dust map.
[h] Flux-averaged magnitude (corrected for interstellar medium extinction as $\langle m \rangle = \langle m \rangle_{\text{not corrected}} - \text{rExt}$.
[i] Heliocentric distance (see Section 3.2).
[j] Oosterhoff type (1 or 2 for RRab stars, 0 for RRc stars).
[k] Substructure group ID (0 for stars not associated with a substructure).

(This table is available in its entirety in machine-readable and Virtual Observatory (VO) forms in the online journal. A portion is shown here for guidance regarding its form and content.)

the procedure from Ses10. The new templates are constructed by interpolating a B-spline through phased light curves of the ∼400 brightest, well-sampled, and visually inspected LINEAR RRab and RRc light curves that do not seem to be affected by Blažko variations. These templates are normalized to the [0, 1] range in magnitude and then fit to all LINEAR RR Lyrae light curves. The final light curve parameters are listed in Table 1.

We emphasize that the point of constructing these templates is simply to provide more accurate model light curves for LINEAR RR Lyrae stars, as these model light curves are used later in the paper. We did not attempt to prune the template set by averaging templates with similar shapes (as done by Ses10), and do not suggest that this new template set should replace the light curve template set constructed by Ses10. However, we do provide the new templates to support future work at extending RR Lyrae template light curves (templates are provided as supplementary data in the online version of the journal).

Table 1 also contains 447 RRab and 336 RRc stars from the LINEAR Catalog of Variable Stars (Palaversa et al. 2013). These RR Lyrae stars were missed by our selection algorithm and are included for completeness. However, they are not used in the analysis below and their exclusion does not significantly change our results.

3.2. Heliocentric Distances

The heliocentric distances of RR Lyrae stars, D, are calculated as

$$D = 10^{(\langle m \rangle - M_{\rm RR})/5+1}/1000\,\text{kpc}, \tag{14}$$

where $\langle m \rangle$ is the flux-averaged LINEAR magnitude and $M_{\rm RR}$ is the absolute magnitude of RR Lyrae stars in the LINEAR bandpass. The flux-averaged magnitude is calculated by first converting the best-fit model light curve, $A\,T(\phi) + m_0$, into flux units (A, $T(\phi)$, and m_0 are the best-fit amplitude, template, and peak brightness, respectively). This curve is then integrated and the result is converted back to magnitudes. The flux-averaged magnitudes, listed in Table 1, are also corrected for interstellar medium extinction $\langle m \rangle = \langle m \rangle_{\text{not corrected}} - \text{rExt}$, where $\text{rExt} = 2.751E(B-V)$ is the extinction in SDSS r band, and $E(B-V)$ color excess is provided by the Schlegel et al. (1998) dust map.

For RRab stars, we adopt $M_{\rm RR} = 0.6 \pm 0.1$ as their absolute magnitude. The absolute magnitude was calculated using the

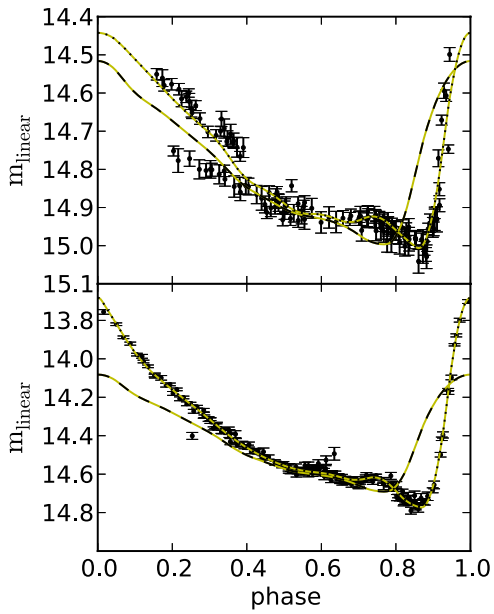

Figure 5. Top: a phased light curve of a Blažko-variable RRab star. The dashed line shows the best-fit template from Ses10, while the dotted line shows the best-fit template created from the LINEAR RRab light curve set. Bottom: an example of an RRab light curve where the best-fit template from Ses10 (dashed line) underestimates the amplitude and does not adequately model the observed data. Note how the best-fit template created from the LINEAR RRab light curve set (dotted line) provides a much better fit.

(A color version of this figure is available in the online journal.)

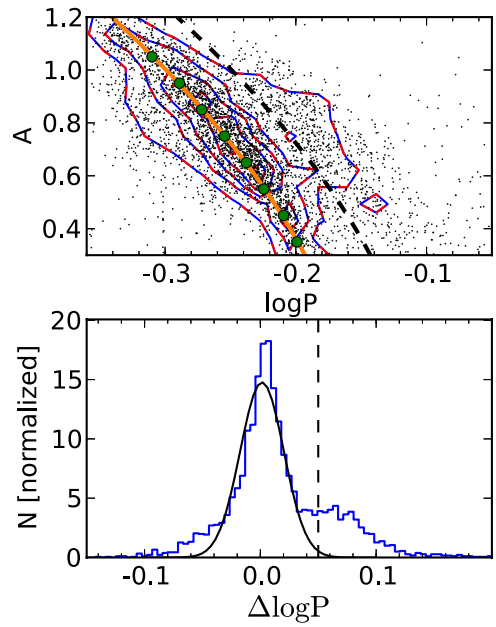

Figure 6. Points in the top panel show the distribution of LINEAR RRab stars in the amplitude vs. period diagram. The linearly spaced contours show 15%–75% of the peak density. The solid line shows the position of the Oo I locus, while the dashed line (offset by $\Delta \log P = 0.05$ from the Oo I locus line) separates the Oo I (to the left) and Oo II RRab stars (to the right). The Oo I locus was obtained by fitting a quadratic line to the median of log periods binned in narrow amplitude bins (solid circles). The position of the dashed line was determined from the $\Delta \log P$ histogram (bottom), where $\Delta \log P$ is the distance (at constant amplitude) from the Oo I locus line. The Gaussian curve in the bottom panel models the peak associated with Oo I RR abs stars, and the vertical dashed line in the bottom panel, centered at $\Delta \log P = 0.05$, tentatively separates Oo I and Oo II RRab stars in this histogram. The short-period tail of the $\Delta \log P$ histogram likely contains Blažko RRab stars. The amplitudes of Blažko RRab stars can be underestimated if they are not observed near the peak of their Blažko cycle (when the light curve amplitude is highest), causing them to scatter downward in this diagram (i.e., toward lower amplitudes at constant periods).

(A color version of this figure is available in the online journal.)

Chaboyer (1999) $M_V - [\mathrm{Fe/H}]$ relation

$$M_V = (0.23 \pm 0.04)[\mathrm{Fe/H}] + (0.93 \pm 0.12), \qquad (15)$$

where we assume that the metallicity of RRab stars is equal to the median metallicity of halo stars ($[\mathrm{Fe/H}] = -1.5$; Ivezić et al. 2008). We also assume that the absolute magnitudes of RRab stars in the LINEAR and Johnson V bandpasses are approximately equal. The estimate of the uncertainty in absolute magnitude is detailed in the next paragraph. For RRc stars, we simply adopt $M_{\rm RR} = 0.5 \pm 0.1$ mag (Kollmeier et al. 2012).

There are three significant sources of uncertainty in the adopted absolute magnitude. First, the $M_{\rm RR} \approx M_V$ approximation is uncertain at ~0.04 mag level (in rms). This uncertainty was estimated by comparing LINEAR and V-band flux-averaged magnitudes of RR Lyrae stars which have multi-epoch data from SDSS Stripe 82. The V-band flux-averaged magnitudes were calculated from synthetic V-band light curves following Section 4.1 by Ses10. Second, the metallicity dispersion in the Galactic halo is about $\sigma_{[\mathrm{Fe/H}]} = 0.3$ dex (Ivezić et al. 2008), and introduces about $\sigma_{M_V}^{[\mathrm{Fe/H}]} = 0.07$ mag of uncertainty due to the assumption that all RRab stars have the same metallicity. And third, there is about $\sigma_{M_V}^{ev} = 0.08$ mag of uncertainty due to RR Lyrae evolution off the zero-age horizontal branch (Vivas & Zinn 2006). By adding all these uncertainties in quadrature, the final uncertainty in the absolute magnitude of RRab stars is about 0.1 mag, implying ~5% fractional uncertainty in distance.

In the rest of this work we only use RRab stars. RRc stars are not used due to their much lower completeness (see Section 2.5 and Figure 3).

4. PERIOD–AMPLITUDE DISTRIBUTION

As suggested by Catelan (2009), the period–amplitude distribution of RR Lyrae stars may hold clues about the formation history of the Galactic halo. Catelan points to a sharp division (a dichotomy first noted by Oosterhoff 1939) in the average period of RRab stars in Galactic globular clusters, $\langle P_{\rm ab} \rangle$; there are Oo I globular clusters with $\langle P_{\rm ab} \rangle \sim 0.55$ days, Oo II globular clusters with $\langle P_{\rm ab} \rangle \sim 0.65$ days, and very few clusters with $\langle P_{\rm ab} \rangle$ in between. On the other hand, the dwarf spheroidal satellite galaxies and their globular clusters fall preferentially on the "Oosterhoff gap" ($0.58 < \langle P_{\rm ab} \rangle < 0.62$; see his Figure 5). Catelan (2009) further argues that, if the Oosterhoff dichotomy is present in the period–amplitude distribution of *field* halo RRab stars, then the Galactic halo could not have been entirely assembled by the accretion of dwarf galaxies resembling the present-day Milky Way satellites. In light of these conclusions, it is interesting to examine the period–amplitude distribution of LINEAR RRab stars and see whether the Oosterhoff dichotomy is also present among the Galactic halo field RRab stars.

A period–amplitude diagram for RRab stars listed in Table 1 is shown in Figure 6. A locus of stars is clearly visible in this diagram. We trace this locus by binning $\log P$ values in narrow amplitude bins, and then calculate the median $\log P$ value in each bin. To model the locus in the $\log P$ versus amplitude diagram, we fit a quadratic function to medians and obtain

$$\log P = -0.16625223 - 0.07021281A - 0.06272357A^2 \qquad (16)$$

as the best fit. The solid line in Figure 6 (top) is very similar to the period–amplitude line of RRab stars in the globular cluster M3 (see Figure 3 by Cacciari et al. 2005). Since M3 is the prototype Oo I globular cluster, we label the main locus as the Oo I locus.

The contours in Figure 6 (top) seem to indicate a presence of a second locus of RRab stars to the right of the Oo I locus. To examine this in more detail, we calculate the period shift, $\Delta \log P$, of RRab stars from the Oo I locus and at a fixed amplitude. The distribution of $\Delta \log P$, shown in Figure 6 (bottom), is centered on zero (the position of the Oo I locus), and has a long-period tail. Even though we do not see the clearly displaced secondary peak that is usually associated with an Oo II component (see Figure 21 by Miceli et al. 2008), hereafter we will refer to stars in the long-period tail as Oo II RRab stars.

To separate the two Oosterhoff types, we model the Oo I peak with a Gaussian and find that this Gaussian roughly ends at $\Delta \log P = 0.05$. RRab stars with $\Delta \log P < 0.05$ (where period is measured in days) are tagged as Oo I RRab stars, and those with $\Delta \log P \geqslant 0.05$ are tagged as Oo II RRab stars. We find the ratio of Oo II to Oo I RRab stars in the halo to be 1:4 (0.25). A similar ratio was found by Miceli et al. (2008) and Drake et al. (2013; 26% and 24%, respectively).

5. NUMBER DENSITY DISTRIBUTION

In this section, we introduce a method for estimating the number density distribution of RR Lyrae stars that is less sensitive to the presence of halo substructures (streams and overdensities). The method is first illustrated and tested on a mock sample of RR Lyrae stars drawn from a known number density distribution. The purpose of this test is to estimate the precision of the method in recovering the input model. At the end of this section, the method is applied to the observed spatial distribution of LINEAR RRab stars.

We begin by drawing 10 mock samples of RRab stars from the following number density distribution:

$$\rho_{\rm model}(X, Y, Z) = \rho_{\odot}^{\rm RR} \left(\frac{R_{\odot}}{r}\right)^{n} \tag{17}$$

$$r = \sqrt{X^2 + Y^2 + (Z/q)^2}, \tag{18}$$

where $\rho_{\odot}^{\rm RR} = 4.5$ kpc^{-3} is the number density of RRab stars at the position of the Sun ($R_{\odot} = 8$ kpc or $(X_{\odot}, Y_{\odot}, Z_{\odot}) = (8, 0, 0)$ kpc), $q = 0.71$ is the ratio of major axes in the Z and X directions indicating that the halo is oblate (flattened in the Z direction), and $n = 2.62$ is the power-law index. The above model was motivated by Jurić et al. (2008), who used a similar model to describe the number density distribution of halo main-sequence stars selected from SDSS. The X, Y, and Z are coordinates in the Cartesian galactocentric coordinate system

$$X = R_{\odot} - D \cos l \cos b, \tag{19}$$

$$Y = -D \sin l \cos b, \tag{20}$$

$$Z = D \sin b, \tag{21}$$

where l and b are Galactic longitude and latitude in degrees, respectively.

The number density model defined by Equation (17) is assumed to be a fair representation of the actual number density distribution of halo RRab stars. The parameters used in the above model were selected based on previous studies of the Galactic halo. Sesar et al. (2011a) have found that a two parameter, single power-law ellipsoid model (i.e., Equation (17)) with $q = 0.71 \pm 0.01$ and $n = 2.62 \pm 0.04$ provides a good description of the number density distribution of halo main-sequence stars within 30 kpc of the Galactic center. Since halo main-sequence stars are progenitors of RR Lyrae stars, it is reasonable to assume that shapes of their number density distributions are similar as well. The number density of RRab stars at the position of the Sun ($\rho_{\odot}^{\rm RR}$) has been estimated by several studies so far, yielding values ranging from 4 to 5 kpc^{-3} (Preston et al. 1991; Suntzeff et al. 1991; Vivas & Zinn 2006).

The mock samples were generated using the *Galfast*[12] code, which provides the position, magnitude, and distance modulus for each star. To simulate the uncertainty in heliocentric distance characteristic of the LINEAR sample of RRab stars, we add Gaussian noise to true distances provided by Galfast (D_0) using a 0.1 mag wide Gaussian centered at zero, $D = D_0 10^{\mathcal{N}(0,0.1)/5}$.

The presence of halo substructure is simulated by adding a clump of about 620 stars to each mock sample (i.e., about 17% of stars are in the substructure) and by distributing them in a uniform sphere 2 kpc wide and centered on $(X, Y, Z) = (8, 0, 10)$ kpc (i.e., roughly in the center of the probed volume of the Galactic halo). Finally, each sample is trimmed down to match the spatial coverage of the LINEAR sample of RRab stars using the following cuts:

$$b > 30^{\circ}, \tag{22}$$

$$\delta_{\rm J2000} < -1.2\,\alpha_{\rm J2000} + 362^{\circ}, \tag{23}$$

$$-4^{\circ} < \delta_{\rm J2000} < 72^{\circ}, \tag{24}$$

$$\delta_{\rm J2000} < 0.73\,\alpha_{\rm J2000} - 26\overset{\circ}{.}6, \tag{25}$$

$$\delta_{\rm J2000} > 1.38\,\alpha_{\rm J2000} - 338\overset{\circ}{.}52, \tag{26}$$

$$5\,{\rm kpc} < D < 23\,{\rm kpc}, \tag{27}$$

$$Z > 3\,{\rm kpc}, \tag{28}$$

where $\alpha_{\rm J2000}$ and $\delta_{\rm J2000}$ are equatorial right ascension and declination in degrees, respectively. The penultimate cut limits the samples to distances where the LINEAR sample of RRab stars is 80% complete, and with the last cut we minimize possible contamination by thick disk stars. Note that mock samples *do not* suffer from any incompleteness or contamination. The reason we are applying the above cuts to mock samples is because the same cuts will later be applied to the observed sample of LINEAR RRab stars, which does suffer from incompleteness at greater distances and may have some contamination from thick disk RRab stars.

The spatial distribution of stars in each mock sample traces the underlying number density distribution. To compute the number density of stars at some XYZ position in the Galactic halo, we use a Bayesian estimator developed by Ivezić et al. (2005; also see Chapter 6.1 of Ivezić et al. 2013):

$$\rho(X, Y, Z) = \frac{3(m+1)}{4\pi} \frac{1}{\sum_{k=1}^{N_{nn}} d_k^3} = \frac{111}{4\pi} \frac{1}{\sum_{k=1}^{8} [(X - X_k)^2 + (Y - Y_k)^2 + (Z - Z_k)^2]^{3/2}}, \tag{29}$$

[12] http://mwscience.net/trac/wiki/galfast

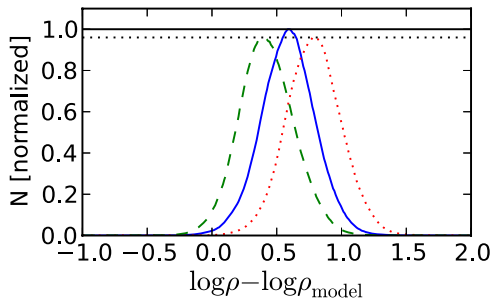

Figure 7. Comparison of $\Delta \log \rho$ histograms obtained with the correct number density model ($q = 0.71$, $n = 2.62$; solid), a model with the wrong power-law index n ($q = 0.71$, $n = 3.1$; dotted), and a model with the wrong oblateness parameter q ($q = 0.9$, $n = 2.62$; dashed). The histograms are normalized to the height of the histogram for the correct model. Note that the height of histograms obtained with incorrect models (dashed and dotted) are lower than the height of the histogram obtained with the correct number density model (solid). The difference in heights, illustrated by the horizontal solid and dotted line, is 4%. For a given q and n, $\rho_\odot^{\rm RR}$ is estimated as the mode of a $\Delta \log \rho$ histogram raised to the power of 10. For example, for the correct model $\rho_\odot^{\rm RR} = 10^{0.65} \sim 4.5$ kpc^{-3}.

(A color version of this figure is available in the online journal.)

where $N_{nn} = 8$ is the number of nearest neighbors to which the distance d in a three-dimensional space is calculated, $m = N_{nn}(N_{nn} + 1)/2 = 36$, and (X_k, Y_k, Z_k) is the position of the kth nearest neighbor in Cartesian galactocentric coordinates. The volume of the Galactic halo probed by LINEAR RR Lyrae stars is binned in $0.1 \times 0.1 \times 0.1$ kpc^3 bins, and the number density is computed for each bin. The bins outside the volume specified by Equations (22)–(28) are removed to minimize edge effects. In total, the number density is calculated for about 6 million bins.

Having calculated number densities on a grid, we can now fit Equation (17) to computed number densities in order to find the best-fit n, q, and $\rho_\odot^{\rm RR}$. Standard χ^2 minimization algorithms (e.g., the Levenberg–Marquardt algorithm; Press et al. 1992) are susceptible to outliers in data, such as unidentified overdensities, and produce biased results unless outliers are removed. Since we would rather avoid ad hoc removal of suspected outliers, we use a fitting method that is instead robust to the presence of outliers.

The basic principle of our fitting method is illustrated in Figure 7. When the correct model is used, the height of the distribution of $\Delta \log \rho = \log \rho - \log \rho_{\rm model}$ values is greater than when an incorrect model is used. The influence of substructures is attenuated because overdense regions have highly positive values of $\Delta \log \rho$ (i.e., they are in the wings of the distribution), and thus have little effect on the height of the $\Delta \log \rho$ distribution. Note that in this method, $\rho_\odot^{\rm RR}$ is not a free parameter; $\rho_\odot^{\rm RR}$ is simply estimated as the mode of the $\Delta \log \rho$ distribution raised to the power of 10.

Due to the sparseness of the sample (i.e., Poisson noise), $\log \rho$ values will have a certain level of uncertainty. This uncertainty, or the average random error in $\log \rho$, can be estimated from the rms scatter of $\Delta \log \rho$ values for the correct model. We find this value to be $\sim$0.2 dex. While the average random error can be decreased by increasing the number of nearest neighbors used when computing the density, the downside is an increase in edge effects if the sample is too sparse.

The best-fit values of n and q parameters are determined by measuring the height of the $\Delta \log \rho$ distribution on a fixed n versus q grid. A "height" map for one of the mock RR Lyrae samples generated using Galfast is shown in Figure 8 (left). Due to the sparseness of the sample (Poisson noise), the best-fit values of n and q parameters will not necessarily be exactly the same as input n and q values. To estimate the *statistical* uncertainty in best-fit n and q parameters due to Poisson noise, we do the fitting on all 10 mock samples and analyze the distribution of best-fit parameters. We find that $\rho_\odot^{\rm RR} = 4.4 \pm 0.6$ kpc^{-3}, $q = 0.73 \pm 0.05$, and $n = 2.63 \pm 0.13$, where the errors represent the rms scatter (recall that the true values are $\rho_\odot^{\rm RR} = 4.5$ kpc^{-3}, $q = 0.71$, and $n = 2.62$).

Finally, we apply the above procedure to the observed sample of LINEAR RRab stars. We find that the distribution of RRab stars in the Galactic halo between 5 and 23 kpc can be modeled as an oblate, single power-law ellipsoid (Equation (17))

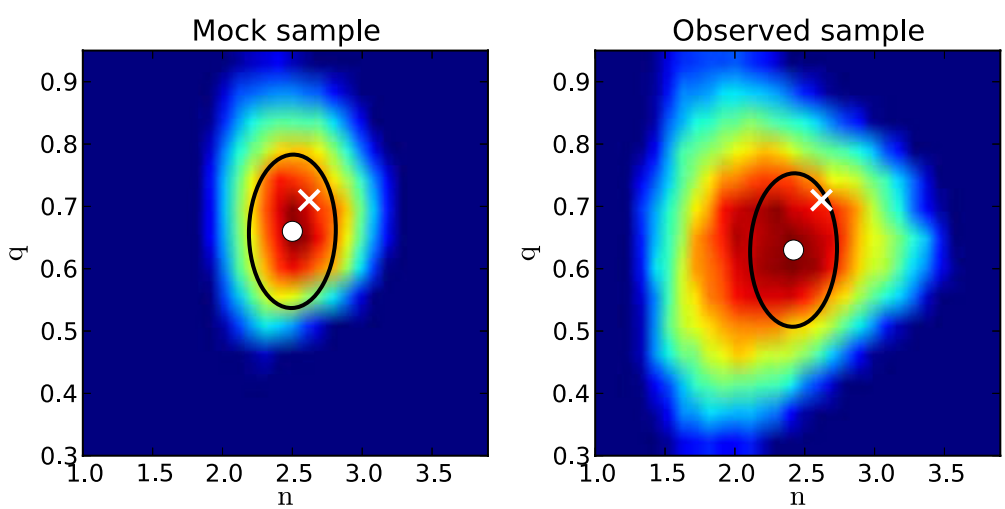

Figure 8. Left: a map showing dependence of the height of the $\Delta \log \rho$ histogram on the assumed oblateness parameter q and power-law index n, for one of the mock RR Lyrae samples generated using Galfast. The color indicates the height of the $\Delta \log \rho$ histogram, with the red color representing the greatest height. The position of the cross symbol indicates the q and n values used by Sesar et al. (2011a) to describe the halo stellar number density within 30 kpc from the Sun. These values ($q = 0.71$, $n = 2.62$) were also used to create mock samples with Galfast. The position of the solid circle indicates the best-fit obtained for this particular mock sample ($q = 0.66$, $n = 2.5$). At this position, the height of the $\Delta \log \rho$ histogram is the greatest. The best-fit and input values are consistent within the 95% confidence limit (ellipse). Right: a height map obtained using the sample of RRab stars observed in LINEAR. The best-fit values of $q = 0.63$ and $n = 2.42$ are consistent with Sesar et al. (2011a) values within the 95% confidence limit (ellipse).

(A color version of this figure is available in the online journal.)

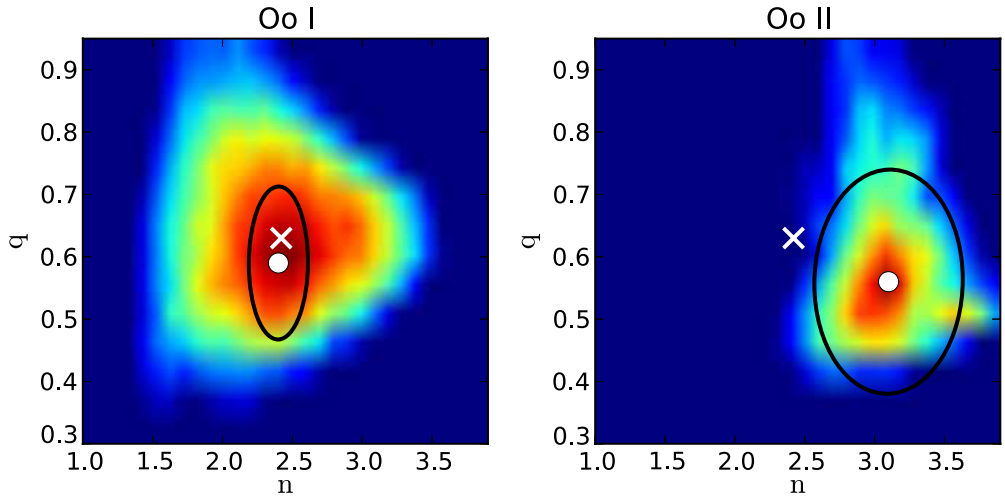

Figure 9. Color-coded "height" maps for the Oosterhoff type I (left) and type II RRab subsamples (right). The "x" marks the best-fit parameters for the full RRab sample ($q = 0.63$, $n = 2.42$), and the solid circle shows the best-fit parameters for the Oo I ($q = 0.59$, $n = 2.4$) and Oo II subsamples ($q = 0.56$, $n = 3.1$). The ellipse indicates the 95% confidence limit.

(A color version of this figure is available in the online journal.)

with the oblateness $q = 0.63 \pm 0.05$ and power-law index $n = 2.42 \pm 0.13$. The uncertainties on these parameters were adopted from the analysis of mock samples described above. The best-fit values are consistent within the 95% confidence limit with values determined by Sesar et al. (2011a) for the number density distribution of halo main-sequence stars ($q = 0.71 \pm 0.01$, $n = 2.62 \pm 0.04$). The number density of RRab stars at the position of the Sun is $\rho_{\odot}^{\rm RR} = 4.5 \pm 0.6$ kpc^{-3}, or $\rho_{\odot}^{\rm RR} = 5.6 \pm 0.8$ kpc^{-3} once the measured number density is increased by 20% to account for completeness of the LINEAR sample of RRab stars (estimated at 80% in Section 2.5). Adopting $q = 0.71$ and $n = 2.62$ from Sesar et al. (2011a), we obtain $\rho_{\odot}^{\rm RR} = 4.9 \pm 0.6$ kpc^{-3}, or $\rho_{\odot}^{\rm RR} = 5.9 \pm 0.8$ kpc^{-3} once the measured number density is increased to account for completeness.

Applying the above procedure to Oo I RRab stars we obtain $q = 0.59 \pm 0.05$, $n = 2.4 \pm 0.09$, and $\rho_{\odot}^{\rm RR} = 4.0 \pm 0.7$ kpc^{-3} ($\rho_{\odot}^{\rm RR} = 5.0 \pm 0.9$ kpc^{-3} when corrected for completeness). For the Oo II subsample, we obtain $q = 0.56 \pm 0.07$, $n = 3.1 \pm 0.2$, and $\rho_{\odot}^{\rm RR} = 2.1 \pm 1.0$ kpc^{-3} ($\rho_{\odot}^{\rm RR} = 2.6 \pm 1.3$ kpc^{-3} when corrected for completeness). The uncertainties on these parameters were adopted from the analysis of mock Oo I and Oo II RRab samples. The "height" maps for the Oo I and Oo II RRab subsamples are shown in Figure 9. These power-law indices are consistent with indices obtained by Miceli et al. (2008) for LONEOS-I Oo I and Oo II RRab subsamples (see their Table 3).

5.1. Rejection of a Simple Power-law Model

The best-fit number density model of the full RRab sample ($n = 2.4$, $q = 0.63$) is consistent with previous models for the number density profiles within 30 kpc from the Galactic center of (1) RR Lyrae stars ($n = 2.4$ assuming $q = 1.0$, Watkins et al. 2009; $n = 2.3$ assuming $q = 0.64$, Sesar et al. 2010a), (2) metal-poor main-sequence stars ($n = 2.6$ and $q = 0.7$, Sesar et al. 2011a), and (3) BHB stars ($n = 2.4$ and $q = 0.6$, Deason et al. 2011). However, a closer inspection of $\Delta \log \rho$ residuals in the R versus Z map (top left panel in Figure 10), indicates that the best-fit single power-law model overestimates the observed number density of RRab stars for $r < 16$ kpc. As shown in Figure 11 (thick solid line), the model at $r \sim 5$ kpc predicts about 3 times more stars than observed.

A possible explanation for this discrepancy could be the incompleteness of the RRab sample at distances closer than 16 kpc. However, this is unlikely as Figure 4 shows the completeness of RRab stars to be about ~80% within 20 kpc. Adding RR Lyrae stars from the LINEAR Catalog of Variable Stars (see the end of Section 3.1) does not alleviate this discrepancy. Another possible explanation is an inadequate model for number density variation with position.

Two simple model modifications include variable oblateness parameter q, and a variable power-law index. The former is not supported by data: when two subsamples selected by $R_{gc} < 12$ kpc and $R_{gc} > 12$ kpc are fit separately, the best-fit q is essentially unchanged. This invariance of oblateness with distance is consistent with several recent studies (Miceli et al. 2008; Sesar et al. 2011a; Deason et al. 2011).

A double power-law model is one possible extension of the single power-law model used above. When a double power-law model with oblateness parameter $q = 0.65 \pm 0.03$, inner power-law index $n_{\rm inner} = 1.0 \pm 0.3$, outer power-law index of $n_{\rm outer} = 2.7 \pm 0.3$, and a break radius at $r_{\rm br} = \sqrt{X^2 + Y^2 + (Z/q)^2} = 16 \pm 1$ kpc is fit to data, the residuals improve, but the model now underestimates the observed number densities within $r \lesssim 10$ (see Figures 10 and 11). Again, the errors on best-fit parameters are statistical uncertainties adopted from the analysis of mock RRab samples, as done in the previous section. The remaining residuals within $r \lesssim 10$ may be (again) due to an inadequate model or they may be due to an overdensity (a diffuse overdensity has been reported in this region; see Figure 12). A power law with an index of $n = 2.5$ can model the residuals within $r \lesssim 10$ fairly well, but that would mean that the number density distribution of RR Lyrae stars in the halo has a much more complicated shape than ever reported (three power laws).

Another possible explanation for the peculiar shape of the observed number density distribution is that the halo does not have a smooth distribution of RR Lyrae stars, with an occasional overdensity imprinted on top of it, but that the distribution is more clumpy. To verify this hypothesis, we generated a mock sample consisting of 400 uniform spheres with a radius of 2 kpc,

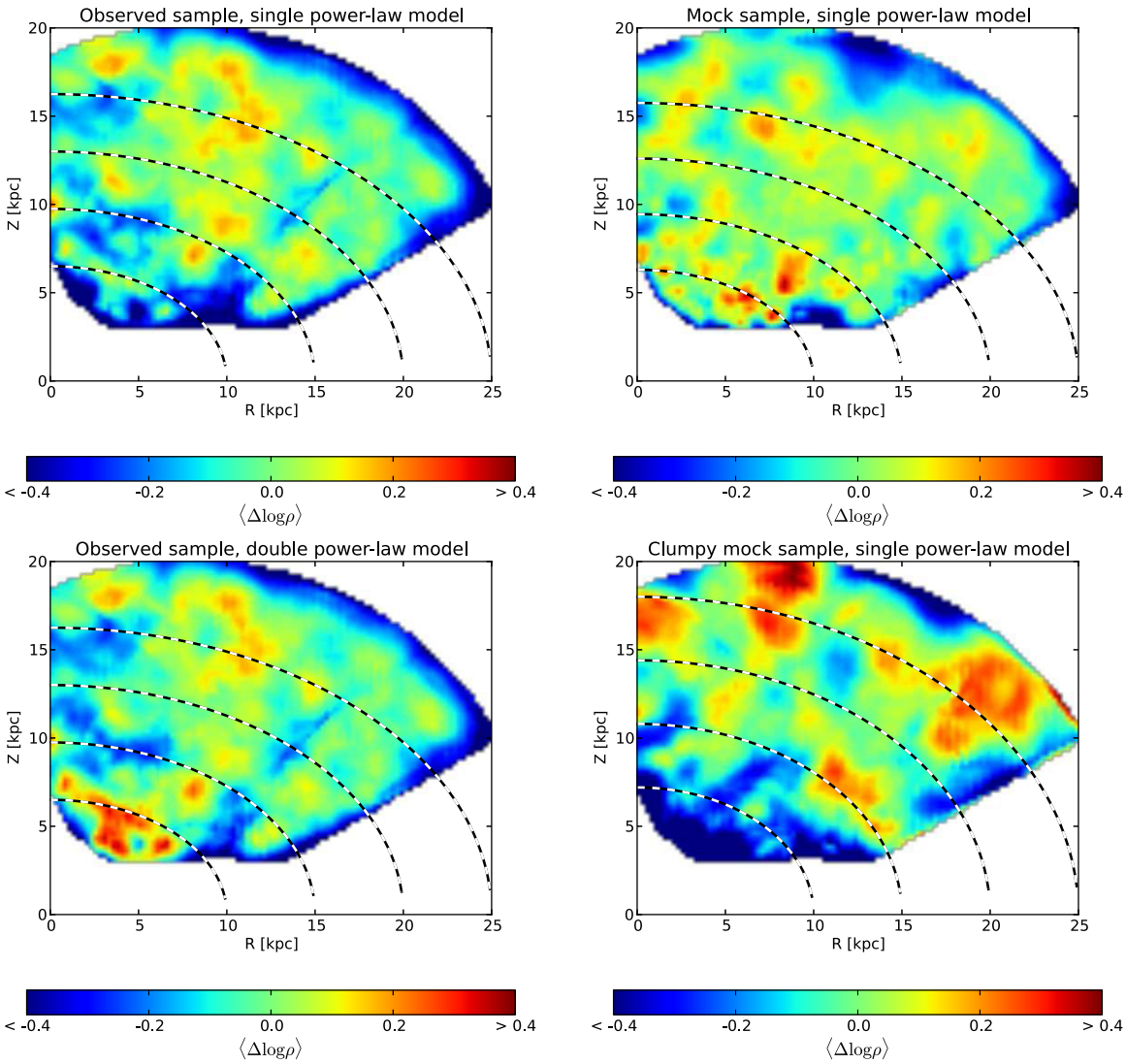

Figure 10. Top left $R = \sqrt{X^2 + Y^2}$ vs. Z map shows median $\Delta \log \rho$ residuals obtained by fitting a $q = 0.63$, $n = 2.42$ single power-law model to the observed number density distribution of the full RRab sample. The residuals are color-coded according to legend. The dashed lines show constant distances $r = \sqrt{X^2 + Y^2 + (Z/q)^2}$ of 10, 15, 20, and 25 kpc. Note how this best-fit single power-law model overestimates the number densities (median $\Delta \log \rho < 0$) for $r < 16$ kpc. For comparison, the top right panel shows residuals obtained by fitting a single power law to the number density distribution of a mock sample drawn from a smooth $q = 0.63$, $n = 2.42$ model. The residuals in this map illustrate the level of shot noise that is also present in the observed sample (top left map). The bottom left map shows the residuals obtained by fitting a double power law to the observed number density distribution of the full RRab sample. The residuals for $10 < r/\mathrm{kpc} < 16$ have decreased, but the model now underestimates the number density within $r \sim 10$ kpc. The bottom right map shows the residuals obtained by fitting a single power law to the number density distribution of a mock sample consisting of 400 uniform clumps (see Section 5.1 for details). Note how the residuals in this map are systematically more negative for $r \lesssim 15$ kpc, a trend that is also present in the observed sample (top left map).

(A color version of this figure is available in the online journal.)

with each sphere containing seven stars. The residuals obtained after fitting a single power-law model to the number density distribution of this clumpy mock sample are shown in Figure 10 (bottom right panel) and Figure 11 (dotted line). As evident from Figure 11, the residuals for the clumpy mock sample and the observed sample exhibit similar trends with $\log r$ when fitted with a single power law. The agreement is qualitative enough to suggest that the shape of the observed number density distribution of RRab stars could be due to a purely clumpy halo.

We have used a broken power law to separately model the number densities of the Oo I and Oo II samples. For the former, the best-fit parameters are the same as for the full sample (recall that Oo I stars account for 75% of the full sample). The best parameters for the Oo II sample are $q = 0.60$, $n_{\mathrm{inner}} = 1.6$, $n_{\mathrm{outer}} = 3.4$, $r_{\mathrm{br}} = 18$ kpc, and $\rho_{\odot}^{\mathrm{RR}} = 0.6 \pm 0.5$ kpc^{-3}. Therefore, for both single and broken power-law models, the number density distribution for the Oo II subsample is steeper than for the Oo I subsample.

6. HALO SUBSTRUCTURES

In the previous section, we used the spatial distribution of LINEAR RRab stars to estimate the best-fit smooth model for their number density distribution. In this section, we use a group-finding algorithm EnLink (Sharma & Johnston 2009) to identify significant clusters of RR Lyrae stars (halo substructures). The search for halo substructures is done using LINEAR RRab stars that pass Equations (22)–(28). The sample of RRab stars is not split by Oosterhoff type so that groups that are "Oosterhoff

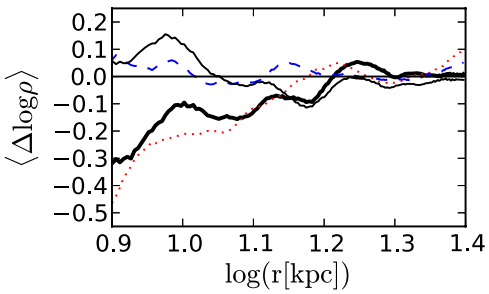

Figure 11. Dependence of median $\Delta \log \rho$ residuals shown in Figure 10 on log of distance $r = \sqrt{X^2 + Y^2 + (Z/q)^2}$. The thick solid line shows the residuals for the top left map (observed sample fitted by a single power law), the dashed line shows the residuals for the top right map (smooth mock sample fitted by a single power law), the thin solid line shows the residuals for the bottom left map (observed sample fitted by a double power law), and the dotted line shows the residuals for the bottom right map (clumpy mock sample fitted by a single power law).

(A color version of this figure is available in the online journal.)

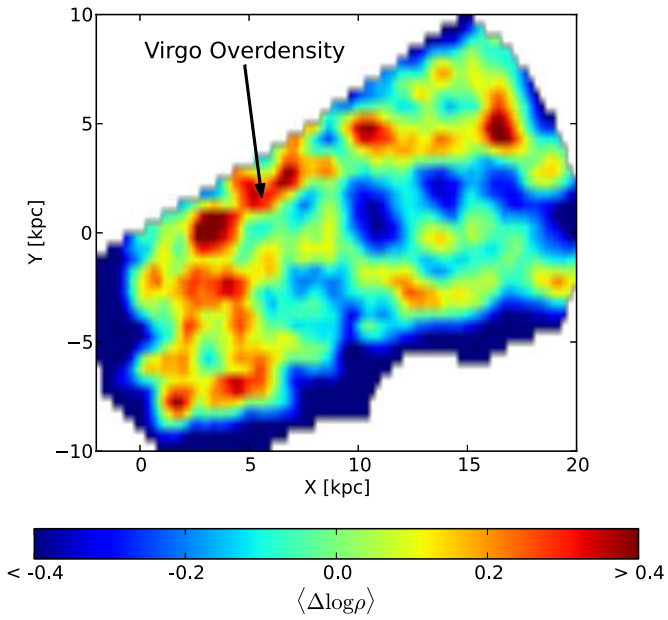

Figure 12. X vs. Y map showing median $\Delta \log \rho$ residuals in the $3 < Z < 7$ kpc range (the vicinity of the Virgo Overdensity; Jurić et al. 2008). The residuals come from a comparison with the best-fit double power-law model.

(A color version of this figure is available in the online journal.)

intermediate," i.e., groups that may be associated with remnants of dSph galaxies, can be detected as well.

The algorithm EnLink has two free parameters which need to be supplied by the user. The first parameter is the number of nearest neighbors employed for density estimation, $k_{\rm den}$. Sharma & Johnston (2009) find that $k_{\rm den} = 30$ is appropriate for most clustering tasks, and we adopt their value. The second parameter is the significance threshold $S_{\rm th}$. Clusters of points that have significance S below threshold $S_{\rm th}$ are denied the status of a group and are merged with the background.

Sharma & Johnston (2009) define the statistical significance S for a group as a ratio of signal associated with a group to the noise in the measurement of this signal. The contrast, $\ln(\rho_{\rm max}) - \ln(\rho_{\rm min})$ between the peak density of a group ($\rho_{\rm max}$) and valley ($\rho_{\rm min}$) where it overlaps with another group can be thought of as the signal, and the noise in this signal is given by the variance $\sigma_{\ln \rho}$ associated with the density estimator ($\sigma_{\ln \rho} = 0.22$ for $k_{\rm den} = 30$). Combining the definitions of signal and noise then leads to $S = (\ln(\rho_{\rm max}) - \ln(\rho_{\rm min}))/\sigma_{\ln \rho}$.

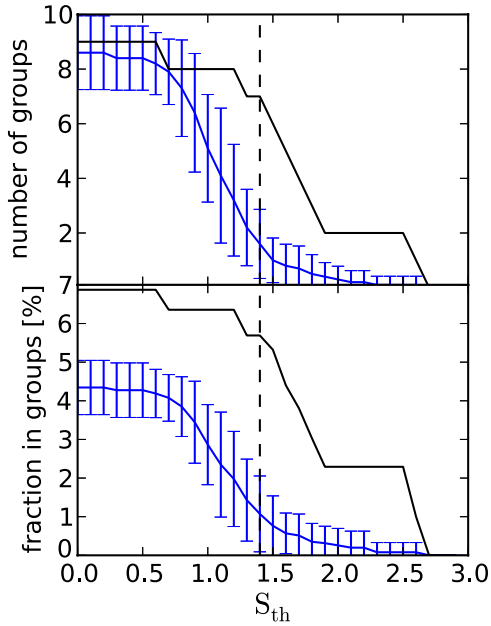

Figure 13. Number of groups (top) and the percentage of stars in groups (bottom) identified by EnLink as a function of significance threshold $S_{\rm th}$. The line with error bars shows the dependence obtained by running EnLink on 10 mock samples of RR Lyrae stars that have no real groups. The error bars show the standard deviation. The line without error bars shows the dependence obtained by running EnLink on the observed sample of LINEAR RRab stars. For $S_{\rm th} = 1.4$ (dashed line), EnLink identifies seven groups in the observed sample and one spurious group in mock samples. In the observed sample, these seven groups contain about 5.5% of all stars in the sample. In the mock samples, the one spurious group contains about 1% of all stars.

(A color version of this figure is available in the online journal.)

Selecting the value of $S_{\rm th}$ is not trivial. For values of $S_{\rm th}$ that are too low, EnLink may detect spurious groups (i.e., groups produced by Poisson noise). On the other hand, a threshold that is too high might miss real halo substructures.

To find the optimal choice of $S_{\rm th}$ for our sample of LINEAR RRab stars, we run EnLink on 10 mock samples of RRab stars drawn from a number density distribution defined by Equation (17), where $n = 2.42$, $q = 0.63$, and $\rho_\odot^{\rm RR} = 4.5\ {\rm kpc}^{-3}$ (the best-fit single power-law model; see Section 5). While this model may not be the best description of the number density distribution of RRab stars in the halo (i.e., it overestimates the number of RRab stars; see Section 5.1), it is still useful. Mock samples drawn from this model will have a higher chance of producing spurious groups (simply because they contain more stars), and thus the number of spurious groups detected in such samples can serve as an upper limit on the number of spurious groups that one may expect to find in the observed sample.

To make mock samples similar to our sample of LINEAR RRab stars, we add noise to heliocentric distances in mock samples and then trim down samples using Equations (22)–(28). The EnLink algorithm is applied to each mock sample and the number of detected groups and the fraction of stars in groups as a function of $S_{\rm th}$ is recorded. The results are shown in Figure 13.

When the significance threshold $S_{\rm th}$ is low ($S_{\rm th} < 0.7$), EnLink detects several groups in mock samples. These groups are spurious, have low significance, and they arise due to Poisson noise. As the threshold $S_{\rm th}$ increases, the number of groups in mock samples decreases (i.e., random fluctuations are not likely to create highly significant groups). The number of groups

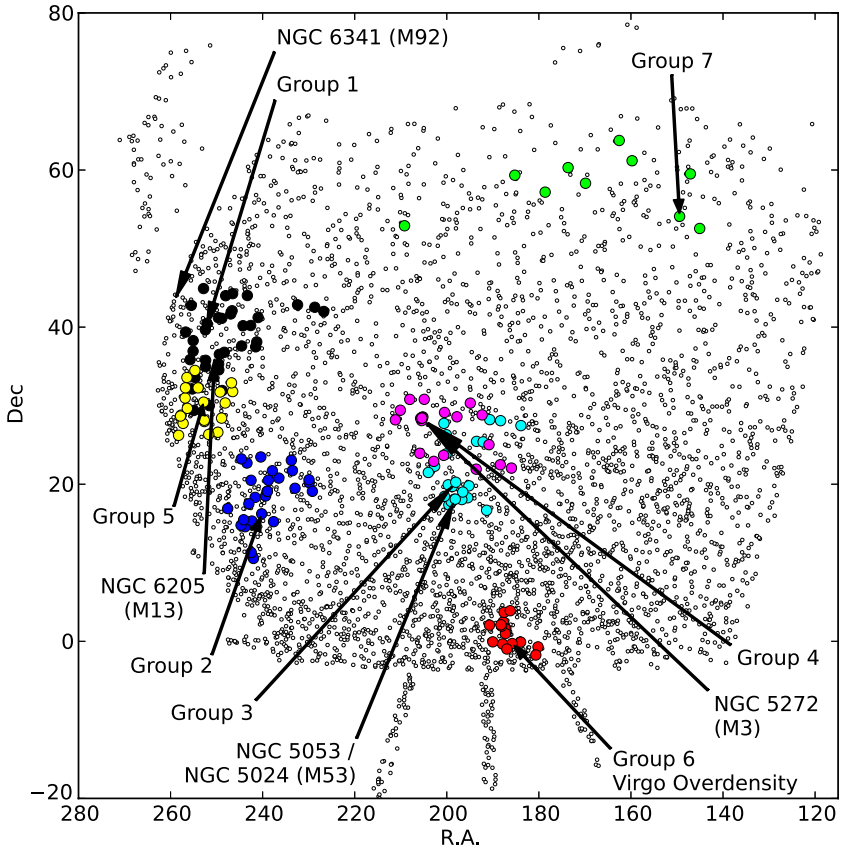

Figure 14. Spatial distribution of 4067 RRab stars selected from the LINEAR survey (small open circles). The solid circles show positions of RRab stars associated with significant groups and arrows point to positions of peaks in number density. Positions of globular clusters in the vicinity of groups are indicated by arrows.

(A color version of this figure is available in the online journal.)

Table 2
Halo Substructures Detected in LINEAR

Group	R.A.[a] (deg)	Decl.[a] (deg)	Distance[a] (kpc)	Radius[b] (kpc)	$N_{\rm stars}$	Significance[c]	Near	$N_{\rm Oo\,II}/N_{\rm Oo\,I}$[d]
1	252.434435	39.649328	10.1	1.3	35	2.58	?	0.52
2	240.211410	16.229577	7.7	1.0	27	2.63	?	0.80
3	198.052741	20.254224	15.7	1.1	25	1.55	NGC 5053 or NGC 5024 (M53)	0.79
4	205.408486	28.409365	10.4	1.0	21	1.77	NGC 5272 (M3)	0.05
5	252.816666	30.449727	6.8	0.7	20	1.88	NGC 6205 (M13)	0.33
6	185.795386	-0.282617	15.4	1.4	16	1.60	Virgo Stellar Stream	0.23
7	149.429078	54.102182	6.0	1.5	10	1.42	?	0.25

Notes.
[a] Right ascension, declination, and the heliocentric distance of the peak in number density, where the number density has been measured by EnLink.
[b] Radius of the group, estimated as the median distance of stars from the peak in number density.
[c] Significance of the group, as measured by EnLink.
[d] Ratio of Oosterhoff type II to Oosterhoff type I RRab stars. For the full LINEAR RRab sample, this ratio is 0.25.

detected in the observed sample also decreases with increasing $S_{\rm th}$, but at a different rate. For $S_{\rm th} = 1.4$, EnLink detects seven groups in the observed sample and on average one (spurious) group in mock samples. By increasing the significance threshold to 2.5, we could eliminate the possibility of detecting a spurious group in the observed sample, but the number of detected groups would drop to two. We select $S_{\rm th} = 1.4$ as the significance threshold; this choice results in one expected spurious group.

The positions of detected groups, number of stars in a group, and significance of a group are listed in Table 2. The spatial distribution of RRab stars associated with these groups is shown in Figures 14 and 15. The stars associated with these groups are also appropriately labeled in Table 1 (see column "Group ID"). On average, the groups have radii of ∼1 kpc, where the radius is the median distance of stars in a group from the peak in number density for that group.

6.1. Detected Groups

Of the seven groups, three groups (groups 3, 4, 5) are near globular clusters (M53 or NGC 5053, M3, and M13), and one group (group 6) is located in the Virgo constellation where several halo substructures have already been reported (Vivas et al. 2001; Newberg et al. 2002; Duffau et al. 2006; Jurić et al.

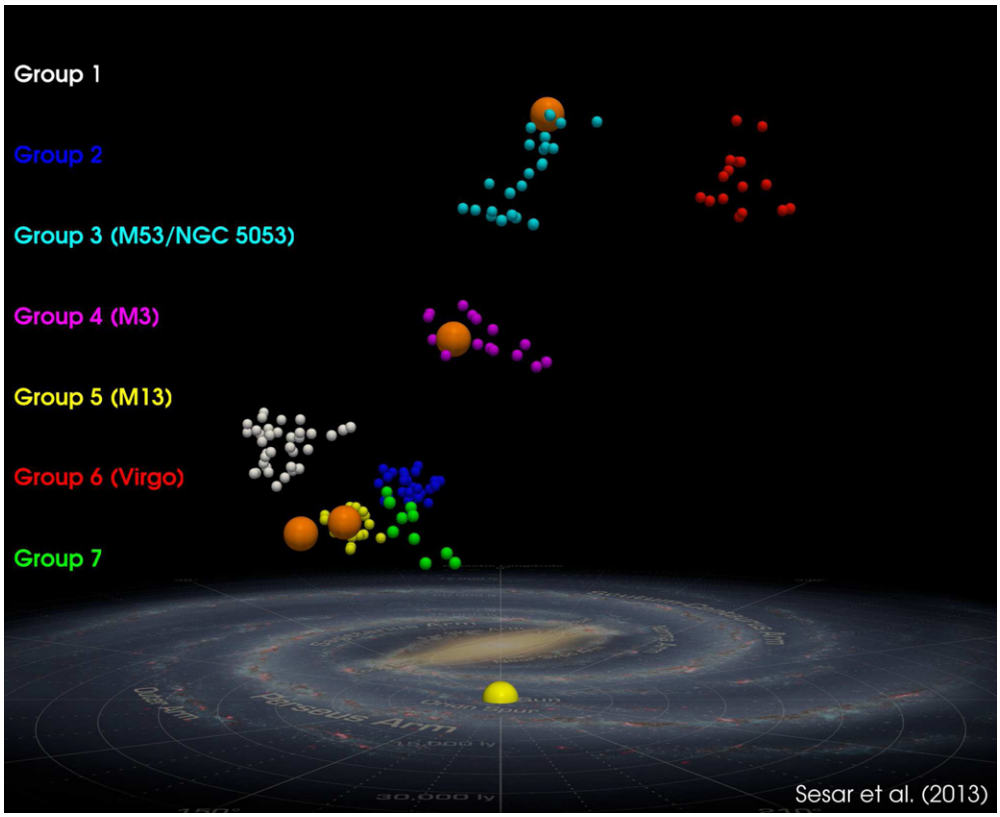

Figure 15. Single frame of an animation showing a fly-by of halo substructures detected in this work and of the scaled Galactic plane (annotated artist's concept by NASA/JPL-Caltech). The small spheres show LINEAR RRab stars associated with significant groups and the larger spheres show the positions of globular clusters in the vicinity of groups. The heliocentric distances of globular clusters, which were taken from the Harris (1996) catalog (2010 edition), have been multiplied by $10^{0.2(0.23[\mathrm{FeH}]+0.93-0.6)}$ to account for the difference between the absolute magnitude of RRab stars in the cluster and the one adopted for all RRab stars in this work ($M_{\mathrm{RR}} = 0.6$; see Section 3.2). Going from left to right, the globular clusters are M92, M13, M3 and M53. No known halo substructures, globular clusters or dSph galaxies are near groups 1, 2, and 7. Note the extended morphology of groups 3 and 4. These groups may trace tidal streams related to, or in the vicinity of, M53 and M3 globular clusters.

(An animation and color version of this figure are available in the online journal.)

2008). The groups 3 and 4 are not isotropic and seem to have a stream-like morphology (Figure 15). For example, group 4, which is located near the globular cluster M3, extends ∼4 kpc roughly parallel to the Galactic plane, and makes ∼45° angle with the Sun–Galactic Center line. Group 3, which is located near globular clusters M53 and NGC 5053, on the other hand, extends more toward the Galactic plane. Previous studies have detected tidal streams around NGC 5053 and M53 (Lauchner et al. 2006; Chun et al. 2010), and no streams have been detected around M3 (Grillmair & Johnson 2006).

The seemingly non-isotropic distribution of RRab stars in group 5, which is near globular cluster M13, is likely due to limited spatial coverage (the group is close to the edge of the probed volume). However, even though this group is near globular cluster M13, its relationship with the cluster is quite tenuous since M13 is known to have a very small number of RR Lyrae stars (Clement et al. 2001).

Groups 1, 2, and 7 do not seem to be near any known halo substructures (e.g., the Sagittarius tidal streams), dSph galaxies or globular clusters. Globular clusters M92 and M13 are the closest clusters to group 1, but they are still off by ∼3 kpc in heliocentric distance. This offset is well outside the uncertainty in distance, especially since the metallicities of clusters are known and can be used to calculate the absolute magnitudes of RRab stars potentially originating from clusters (using Equation (15)). Group 7 contains only 10 RRab stars and has borderline significance ($S = 1.42$). Thus, this group is the one most likely to be spurious.

The ratio of Oo II to Oo I RRab stars in a group may provide additional clues on the nature of detected groups. As shown in Section 4, this ratio is 1:4 for the halo. For group 4, this ratio is close to zero (0.05; see Table 2), indicating that the group 4 is dominated by Oo I RRab stars. This result is interesting because M3 is classified as an Oo I-type globular cluster (Catelan 2009) and is located within group 4 (see bottom panel in Figure 16). Thus, the fact that the group 4 and the globular cluster M3 have the same Oosterhoff type may indicate their common origin.

Group 3 is near globular clusters NGC 5053 and M53, both of which are classified as Oo II-type globular clusters (Catelan 2009). Again, we find many more Oo II RRab stars from this group near the centers of globular clusters NGC 5053 and M53 (bottom panel in Figure 17), and the group as a whole has a higher ratio of Oo II to Oo I RRab stars (0.79). The reason we are not detecting more Oo II RRab stars and the reason this ratio is not much higher for this particular group is due to the incompleteness of the LINEAR RRab sample in crowded regions (e.g., near centers of globular clusters).

Group 3 may actually consist of two groups of stars that were joined by EnLink into a single group. Looking at group 3 in Figure 15, we can discern a "stream" of points that is parallel to the Galactic plane, and spans ∼4 kpc at ∼13.5 kpc above the Galactic plane. The ratio of Oo II to I types in this subgroup

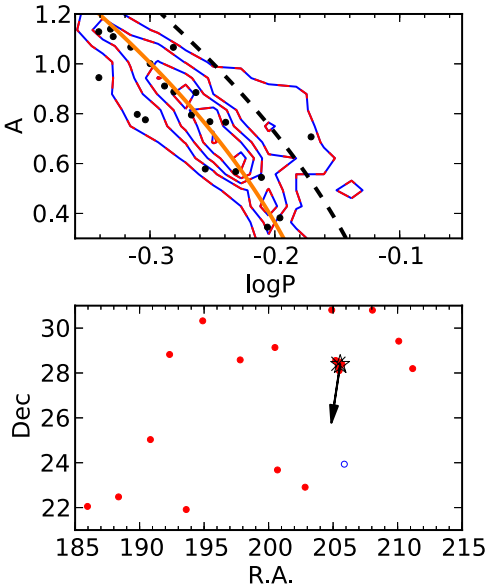

Figure 16. Distribution of RRab stars from group 4 in the amplitude vs. period diagram (top) and right ascension vs. declination plot (bottom). The contours, solid, and dashed lines are the same as in Figure 6. The "x" symbol shows the position of the peak in number density and the (overlapping) open star symbol shows the position of globular cluster M3 according to the Harris (1996) catalog (2010 edition). The arrow indicates the proper motion of M3 ($\mu_\alpha \cos\delta = -0.06 \pm 0.3$ mas yr^{-1}, $\mu_\delta = -0.26 \pm 0.3$ mas yr^{-1}; Wu et al. 2002). Oosterhoff type I (Oo I) and Oosterhoff type II (Oo II) RRab stars are shown as solid and open circles, respectively. The 6 RRab stars located near the center of M3 are known cluster members (Clement et al. 2001). In the bottom panel, the extended distribution of RRab stars well outside the cluster's 30′ tidal radius suggests presence of a possible tidal stream.

(A color version of this figure is available in the online journal.)

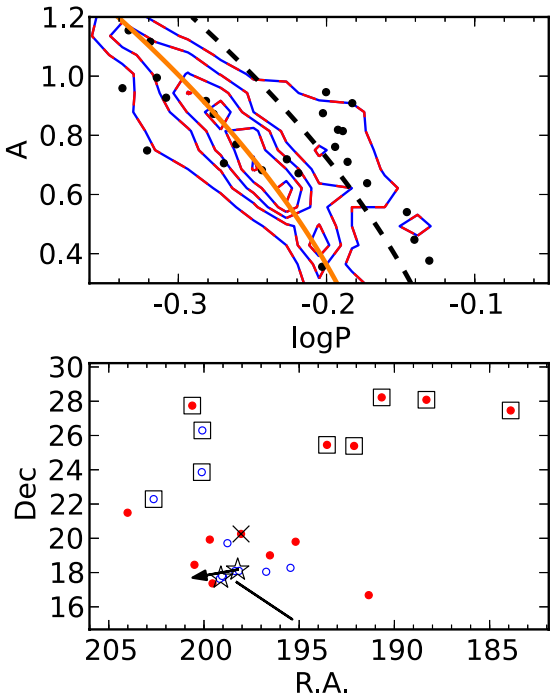

Figure 17. Similar to Figure 16, but for RRab stars from group 3. The open star symbols shows the positions of globular clusters NGC 5053 (left) and M53 (right) according to the Harris (1996) catalog (2010 edition). The solid line shows the extent of the NGC 5053 tidal stream reported by Lauchner et al. (2006), and the arrow indicates the proper motion of M53 ($\mu_\alpha \cos\delta = 0.5 \pm 1.0$ mas yr^{-1}, $\mu_\delta = -0.1 \pm 1.0$ mas yr^{-1}; Odenkirchen et al. 1997). The proper motion of NGC 5053 has not yet been reported. Presence of a significant number of Oo II RRab stars in this group (open circles) and their proximity to centers of Oo II-type globular clusters M53 and NGC 5053 further strengthen the association of at least a part of group 3 with these globular clusters. The circles enclosed in squares are stars located between 13 and 14 kpc from the Galactic plane. These stars are evident as a "stream" of points in group 3 that is parallel to the Galactic plane and that spans ∼4 kpc (see Figure 15). The ratio of Oosterhoff II to I types in this subgroup is 1:2. Based on its morphology, this subgroup may be a separate halo substructure that EnLink joined with the NGC 5053/M53 group of RRab stars.

(A color version of this figure is available in the online journal.)

is 1:2, or higher than in the halo. Based on the morphology of this subgroup and its distance from the globular clusters M53 and NGC 5053 (∼2–3 kpc), this subgroup may be a separate halo substructure that EnLink joined with the NGC 5053/M53 group of RRab stars.

It is worth mentioning that although M53 and NGC 5053 are relatively close to each other in space, they have radial velocities that differ by more than 100 km s^{-1} (Harris 1996 catalog, 2010 edition). Follow-up spectroscopic studies should take advantage of this fact when associating group 3 and its parts with either of these globular clusters.

In principle, the proper motions of clusters could be used to identify RR Lyrae stars that were tidally stripped, as such stars would follow the motion of the clusters. In the case of M53 and NGC 5053, there are a few RR Lyrae stars near R.A. $\sim 196°$ and Decl. $\sim 19°$ (see the bottom panel of Figure 17) that roughly align with the proper motion vector of M53 and with the tidal stream reported by Lauchner et al. (2006). These stars may have been tidally stripped and may be trailing M53 or NGC 5053. However, since the proper motion of M53 is quite uncertain ($\mu_\alpha \cos\delta = 0.5 \pm 1.0$ mas yr^{-1}, $\mu_\delta = -0.1 \pm 1.0$ mas yr^{-1}; Odenkirchen et al. 1997), and since the proper motion of NGC 5053 has not yet been reported, it is difficult to judge whether this is truly the case. In the case of M3, the RR Lyrae stars in group 4 spread in the east–west direction (see the bottom panel of Figure 16), or almost perpendicular to the proper motion vector of M3 ($\mu_\alpha \cos\delta = -0.06 \pm 0.3$ mas yr^{-1}, $\mu_\delta = -0.26 \pm 0.3$ mas yr^{-1}; Wu et al. 2002). While this observation could be used as an argument against the claim that the extended parts of group 4 share a common origin with the globular cluster M3, we do point out that the measured proper motion of M3 is still quite uncertain.

Group 6, which is located in the Virgo constellation where several halo substructures have been reported so far, has the ratio of Oosterhoff types that is consistent to the one found for the halo (0.23 versus 0.25).

Groups 1 and 2 have Oosterhoff types ratios that are higher by a factor of 2 and 3, respectively, relative to the halo. Assuming that the number density distributions of Oo I and Oo II RRab stars in the halo are the same, the probabilities of drawing groups 1 and 2 are 0.07 and 0.01. For comparison, the probability of drawing group 6 (in the Virgo constellation) is 0.21, 0.28 for group 7, and 0.23 for the subgroup of group 3.

7. DISCUSSION AND CONCLUSIONS

This paper is the second one in a series based on light curve data collected by the asteroid LINEAR survey. In the first paper, Sesar et al. (2011b) described the LINEAR survey and photometric recalibration based on SDSS stars acting as a dense grid of standard stars. Here, we searched the LINEAR data set for variable RR Lyrae stars and used them to study the Galactic halo structure and substructures.

While this paper was in preparation, a study of RR Lyrae stars selected from the Catalina Surveys Data Release 1 (CSDR1) was announced (Drake et al. 2013). The two works are largely complementary in terms of science; while Drake et al. analyzed radial velocity and metallicity distributions of CSDR1 RR Lyrae stars with spectroscopic measurements from SDSS and focused on the Sagittarius stream, we searched for new halo substructures and studied the number density distribution of RR Lyrae stars as a whole and by Oosterhoff type.

In total, we have selected 4067 RRab and 834 RRc stars from the recalibrated LINEAR data set. These stars probe ∼8000 deg^2 of sky to 30 kpc from the Sun. The LINEAR sample of RR Lyrae stars has low contamination (∼2%) and is ∼80% complete to 23 kpc from the Sun. To facilitate follow-up studies, the coordinates and light curve properties (amplitude, period, etc.) of stars in this sample are made publicly available, as well as their Oosterhoff classification and whether they are associated with a halo substructure.

We also provide light curve templates that were derived from phased light curves of ∼400 bright LINEAR RRab and RRc stars. Even though we used these templates to obtain more accurate model light curves of LINEAR RR Lyrae stars, we emphasize that we did not attempt to prune the template set by averaging templates with similar shapes (as done by Ses10), and do not suggest that this new template set should replace the light curve template set constructed by Ses10. However, we do provide the new templates to support future work at extending RR Lyrae template light curves (templates are provided as supplementary data in the online version of the journal).

We find evidence for the Oosterhoff dichotomy among field RR Lyrae stars. While we do not see the clearly displaced secondary peak in the $\Delta \log P$ diagram (bottom panel in Figure 6) that is usually associated with an Oo II component (e.g., see Figure 21 by Miceli et al. 2008), we do detect a long tail that contains RRab stars with periods consistent with Oo II RRab stars. The ratio of the number of stars in the Oo II and I subsamples is 1:4. A similar ratio was found by Miceli et al. (2008) and Drake et al. (2013; 0.26 and 0.24, respectively).

The lack of a clear gap in the $\Delta \log P$ distribution between the two components may be a combination of two factors. First, this region in the $\Delta \log P$ diagram may contain "Oosterhoff intermediate" RR Lyrae stars. As these stars are presumed to come from dwarf galaxies similar to present-day Milky Way dSph satellite galaxies (Catelan 2009), the lack of a gap may be evidence that some fraction of stars were accreted from such systems. Second, the gap may be filled by short-period Oo II RR Lyrae stars that are undergoing Blažko variations. If they are not observed at the maximum of their Blažko cycle when their light curve amplitude is the greatest, or if their maximum light curve amplitude is not recognized in the folded data, these stars will scatter toward lower amplitudes at the same period and will fill in the gap between the two Oosterhoff components.

The wide coverage and depth of the LINEAR RRab sample allowed us to study the number density distribution of halo RRab stars to a much greater extent than it was possible in previous studies. We find it possible to describe the number density of RRab stars by an oblate $1/r^n$ ellipsoid, with the axis ratio $q = 0.63$ and the power-law index of $n = 2.42$. These values are consistent with previous models for the number density of various tracers within 30 kpc from the Galactic center (Watkins et al. 2009; Sesar et al. 2010a, 2011a; Deason et al. 2011).

However, as discussed in Section 5.1 and as illustrated in Figure 18, the single power-law model overestimates the number density of RRab stars within $r \sim 16$ kpc. Analysis done in Section 2.5 excludes incompleteness as a likely explanation for this discrepancy. Potential problems with the fitting method are also unlikely, as we have repeatedly tested our fitting method on several mock samples drawn from known number density distributions, and have quantified its precision in recovering input parameters in the presence of realistic distance errors and halo substructures. The discrepancy between the best-fit single power-law model and the observed number density can be decreased by using a broken (or double) power-law model, where the power-law index changes from $n_{\rm inner} = 1.0$ to $n_{\rm outer} = 2.7$ at the break radius of $r_{\rm br} \sim 16$ kpc, with the best-fit oblateness parameter set at $q = 0.65$. The variation in the power-law index is not due to the smaller Oo II component, because this subsample also shows independent evidence for a variable power law. Alternatively, as simulations with mock samples have suggested, the observed variable power-law slope may not due to a change in the smooth distribution of stars, but may be evidence of a clumpy distribution of RR Lyrae stars within $r \sim 16$ kpc.

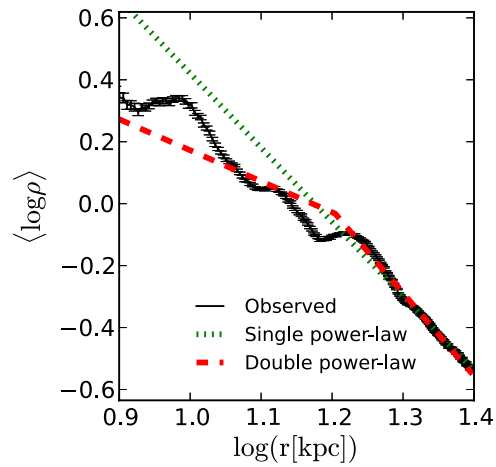

Figure 18. Comparison of the median observed and model log number densities as a function of log distance r. The error bars show the error in the median observed log ρ. The best-fit single power-law model has oblateness parameter $q = 0.63$ and power-law index $n = 2.42$, while the double (or broken) power law has oblateness parameter $q = 0.65$ and a power-law index changing from $n_{\rm inner} = 1.0$ to $n_{\rm outer} = 2.7$ at $r_{\rm br} \sim 16$ kpc.

(A color version of this figure is available in the online journal.)

Possible independent evidence that may support the density profile observed in Figure 18 may be found in a recent kinematic study by Kafle et al. (2012). Kafle et al. used 4667 BHB stars selected from the SDSS/SEGUE survey to determine key dynamical properties of the Galactic halo, such as the profile of velocity anisotropy β

$$\beta = 1 - \frac{\sigma_\theta^2 + \sigma_\phi^2}{2\sigma_r^2}, \tag{30}$$

where σ_r, σ_θ, and σ_ϕ are the velocity dispersions in spherical coordinates. They find that "from a starting value of $\beta \approx 0.5$ in the inner parts ($9 < r/\mathrm{kpc} < 12$), the profile falls sharply in the range $r \approx 13$–18 kpc, with a minimum value of $\beta = -1.2$ at $r = 17$ kpc, rising sharply at larger radius." The metal-rich and metal-poor population of BHB stars analyzed by Kafle et al. (2013) were also found to exhibit similar behavior in β. The range of distances where the β sharply falls is the same range where we find that a shallower power law with an index of 1.0 provides as better fit to observed number densities of RRab

stars. This suggests that the two effects may be related to each other and may have a common cause (e.g., presence of a diffuse substructure).

Using a group-finding algorithm EnLink, we searched for halo substructures in our sample of RRab stars and detected seven candidate halo groups, one of which may be spurious (based on a comparison with mock samples). Three of these groups are near globular clusters (groups 3, 4, and 5), and one (group 6) is near a known halo substructure (Virgo Stellar Stream; Vivas et al. 2001; Duffau et al. 2006). The extended morphology and the position (outside the tidal radius) of some of the groups near globular clusters are suggestive of tidal streams possibly originating from globular clusters. The remaining three groups do not seem to be near any known halo substructures or globular clusters. Out of these, groups 1 and 2 have a higher ratio of Oo II to Oo I RRab stars than what is found in the halo.

While we have done our best to quantify the significance of detected halo groups, we emphasize that these groups are just candidates whose authenticity still needs to be verified. This verification can be done by analyzing metallicities and velocities of RR Lyrae stars obtained from a spectroscopic follow-up (e.g., Sesar et al. 2010b, 2012). If a spatial group is real, then its stars should also cluster in the velocity and metallicity space. Such follow-up studies are highly encouraged and should provide more conclusive evidence on the nature of detected groups.

In this work, we used the sample of LINEAR RR Lyrae stars to study the halo structure and substructures, but its usefulness goes beyond these simple applications. For example, light curves of LINEAR RRab stars are well sampled and should allow a robust decomposition into a Fourier series. In turn, the Fourier components can be used to estimate the metallicity of RRab stars via the Jurcsik & Kovacs (1996) method. These metallicities can then be used to study the metallicity distribution of RR Lyrae stars in the halo. Searches for halo substructures will also benefit from having metallicities as these represent an additional dimension for clustering algorithms such as EnLink. As RRab stars in this sample are brighter than 17 mag, they will be observed by the upcoming surveys such as the LAMOST Experiment for Galactic Understanding and Exploration (LEGUE; Deng et al. 2012) and *Gaia* (Perryman 2002). These surveys will provide metallicity, proper motion, and parallax measurements for RR Lyrae stars up to 30 kpc from the Sun and will enable unprecedented studies of the structure, formation and the evolution of the Galactic halo.

B.S. is grateful for NSF grant AST-0908139 to Judith G. Cohen for partial support. Ž.I. acknowledges support by NSF grants AST-0707901 and AST-1008784 to the University of Washington, by NSF grant AST-0551161 to LSST for design and development activity, and by the Croatian National Science Foundation grant O-1548-2009. A.C.B. acknowledges support from NASA ADP grant NNX09AC77G. The LINEAR program is funded by the National Aeronautics and Space Administration at MIT Lincoln Laboratory under Air Force Contract FA8721-05-C-0002. Opinions, interpretations, conclusions, and recommendations are those of the authors and are not necessarily endorsed by the United States Government.

REFERENCES

Blažko, S. 1907, AN, 175, 325
Buchler, J. R., & Kolláth, Z. 2011, ApJ, 731, 24
Bullock, J. S., Kravtsov, A. V., & Weinberg, D. H. 2001, ApJ, 548, 33
Cacciari, C., Corwin, T. M., & Carney, B. W. 2005, AJ, 129, 267
Catelan, M. 2009, Ap&SS, 320, 261
Chaboyer, B. 1999, in Post-Hipparcos Cosmic Candles, ed. A. Heck & F. Caputo (ASSL, Vol. 237; Dordrecht: Kluwer), 111
Chadid, M., Benkő, J. M., Szabó, R., et al. 2010, A&A, 510, A39
Chun, S.-H., Kim, J.-W., Sohn, S. T., et al. 2010, AJ, 139, 606
Clement, C. M., Muzzin, A., Dufton, Q., et al. 2001, AJ, 122, 2587
De Lee, N. 2008, PhD thesis, Michigan State Univ.
Deason, A. J., Belokurov, V., & Evans, N. W. 2011, MNRAS, 416, 2903
Deason, A. J., Belokurov, V., Evans, N. W., & An, J. 2012, MNRAS, 424, L44
Deng, L.-C., Newberg, H. J., Liu, C., et al. 2012, RAA, 12, 735
Drake, A. J., Catelan, M., Djorgovski, S. G., et al. 2013, ApJ, 763, 32
Duffau, S., Zinn, R., Vivas, A. K., et al. 2006, ApJL, 636, L97
Freeman, K., & Bland-Hawthorn, J. 2002, ARA&A, 40, 487
Friedman, J. H. 1984, A Variable Span Scatterplot Smoother, Tech. Rep., Laboratory for Computational Statistics, Stanford University, Technical Report No. 5
Grillmair, C. J., & Johnson, R. 2006, ApJL, 639, L17
Harding, P., Morrison, H. L., Olszewski, E. W., et al. 2001, AJ, 122, 1397
Harris, W. E. 1996, AJ, 112, 1487
Helmi, A. 2008, A&ARv, 15, 145
Helmi, A., & White, S. D. M. 1999, MNRAS, 307, 495
Ivezić, Ž., Beers, T. C., & Jurić, M. 2012, ARA&A, 50, 251
Ivezić, Ž., Connoly, A., VanderPlas, J., & Gray, A. 2013, Statistics, Data Mining, and Machine Learning in Astronomy: A Practical Guide for the Analysis of Survey Data (Princeton, NJ: Princeton Univ. Press)
Ivezić, Ž., Goldston, J., Finlator, K., et al. 2000, AJ, 120, 963
Ivezić, Ž., Sesar, B., Jurić, M., et al. 2008, ApJ, 684, 287
Ivezić, Ž., Vivas, A. K., Lupton, R. H., & Zinn, R. 2005, AJ, 129, 1096
Johnston, K. V., Bullock, J. S., Sharma, S., et al. 2008, ApJ, 689, 936
Johnston, K. V., Hernquist, L., & Bolte, M. 1996, ApJ, 465, 278
Jurcsik, J., & Kovacs, G. 1996, A&A, 312, 111
Jurić, M., Ivezić, Ž., Brooks, A., et al. 2008, ApJ, 673, 864
Kafle, P. R., Sharma, S., Lewis, G. F., & Bland-Hawthorn, J. 2012, ApJ, 761, 98
Kafle, P. R., Sharma, S., Lewis, G. F., & Bland-Hawthorn, J. 2013, MNRAS, 430, 2973
Keller, S. C., Murphy, S., Prior, S., Da Costa, G., & Schmidt, B. 2008, ApJ, 678, 851
Kinemuchi, K., Smith, H. A., Woźniak, P. R., & McKay, T. A. ROTSE Collaboration. 2006, AJ, 132, 1202
Kolenberg, K., Bryson, S., Szabó, R., et al. 2011, MNRAS, 411, 878
Kollmeier, J. A., Szczygiel, D. M., Burns, C. R., et al. 2012, ApJ, submitted (arXiv:1208.2689)
Lauchner, A., Powell, W. L., Jr., & Wilhelm, R. 2006, ApJL, 651, L33
Mayer, L., Moore, B., Quinn, T., Governato, F., & Stadel, J. 2002, MNRAS, 336, 119
Miceli, A., Rest, A., Stubbs, C. W., et al. 2008, ApJ, 678, 865
Newberg, H. J., Yanny, B., Rockosi, C., et al. 2002, ApJ, 569, 245
Odenkirchen, M., Brosche, P., Geffert, M., & Tucholke, H.-J. 1997, NewA, 2, 477
Oosterhoff, P. T. 1939, Obs, 62, 104
Palaversa, L., Ivezić, Ž., Loebman, S., et al. 2013, AJ, submitted
Perryman, M. A. C. 2002, Ap&SS, 280, 1
Press, W., Flannery, B., Teukolsky, S., & Vetterling, W. 1992, Numerical Recipes in C: The Art of Scientific Computing (Cambridge: Cambridge Univ. Press)
Preston, G. W., Shectman, S. A., & Beers, T. C. 1991, ApJ, 375, 121
Reimann, J. D. 1994, PhD thesis, Univ. of California, Berkeley
Schlegel, D. J., Finkbeiner, D. P., & Davis, M. 1998, ApJ, 500, 525
Sesar, B., Cohen, J. G., Levitan, D., et al. 2012, ApJ, 755, 134
Sesar, B., Ivezić, Ž., Grammer, S. H., et al. 2010a, ApJ, 708, 717
Sesar, B., Ivezić, Ž., Lupton, R. H., et al. 2007, AJ, 134, 2236
Sesar, B., Jurić, M., & Ivezić, Ž. 2011a, ApJ, 731, 4
Sesar, B., Stuart, J. S., Ivezić, Ž., et al. 2011b, AJ, 142, 190
Sesar, B., Vivas, A. K., Duffau, S., & Ivezić, Ž. 2010b, ApJ, 717, 133
Sharma, S., & Johnston, K. V. 2009, ApJ, 703, 1061
Sharma, S., Johnston, K. V., Majewski, S. R., Bullock, J., & Muñoz, R. R. 2011, ApJ, 728, 106
Skrutskie, M. F., Cutri, R. M., Stiening, R., et al. 2006, AJ, 131, 1163
Smith, H. 2004, RR Lyrae Stars (Cambridge Astrophysics; Cambridge: Cambridge Univ. Press)
Sódor, Á., Jurcsik, J., Szeidl, B., et al. 2011, MNRAS, 411, 1585
Suntzeff, N. B., Kinman, T. D., & Kraft, R. P. 1991, ApJ, 367, 528
Süveges, M., Sesar, B., Váradi, M., et al. 2012, MNRAS, 424, 2528
Szczygieł, D. M., Pojmański, G., & Pilecki, B. 2009, AcA, 59, 137
Vivas, A. K., & Zinn, R. 2006, AJ, 132, 714
Vivas, A. K., Zinn, R., Andrews, P., et al. 2001, ApJL, 554, L33
Watkins, L. L., Evans, N. W., Belokurov, V., et al. 2009, MNRAS, 398, 1757
Wu, Z.-Y., Wang, J.-J., & Chen, L. 2002, ChJAA, 2, 216